E-9273

Contract NAS3-25140

Final Report
1 August 1995

Sensors for Ceramic Components in Advanced Propulsion Systems

Task 4 – Sensor System Design and Test Plan Formulation

Task 5 – Fabrication of Sensor Systems

Task 6 – Performance of Tests and Analysis of Results

for the Period April 1987 to August 1994

Prepared for
National Aeronautics and Space Administration
Lewis Research Center
21000 Brookpark Road
Cleveland, Ohio 44135

Prepared by
AC Koller
WH Bennethum
SD Burkholder
RR Brackett
JP Harris

GE Aircraft Engines
Product Test Center
Cincinnati, Ohio 45215

GE Aircraft Engines
One Neumann Way
Cincinnati, Ohio 45215-6301

Contract NAS3-25140
August 1995

Final Report

Sensors for Ceramic Components in Advanced Propulsion Systems

Task 4 – Sensor System Design and Test Plan Formulation
Task 5 – Fabrication of Sensor Systems
Task 6 – Performance of Tests and Analysis of Results

Prepared for
National Aeronautics and Space Administration
Lewis Research Center
21000 Brookpark Road
Cleveland, Ohio 44135

Table of Contents

Section			Page
1.0	**Introduction**		1
2.0	**Platinum Rhodium Thin Film Thermocouple**		2
2.1	Coating Development – Phase 1		2
	2.1.1	Test Plan	2
	2.1.2	Initial Results	4
	2.1.3	Two Step Process	4
2.2	Coating Development – Phase 2		5
	2.2.1	1371°C Heat Treat	7
	2.2.2	Surface Roughness Measurements	8
	2.2.3	Auger Analysis	9
	2.2.4	Conclusions	9
2.3	Coating Development – Phase 3		9
	2.3.1	Post-Process Anneal	10
2.4	Thermocouple Fabrication and Testing		14
	2.4.1	Test Setup	14
	2.4.2	Test Results	15
		2.4.2.1 Thermocouple Endurance	16
		2.4.2.2 Thermocouple Calibration	16
		2.4.2.3 Thermocouple Drift	19
2.5	Conclusions		19
3.0	**Silicon Carbide Thin Film Thermocouple**		21
3.1	Background		21
3.2	Concept Validation		21
3.3	Thin Film Sensor Fabrication		22
	3.3.1	Silicon Nitride Insulating Films	23
	3.3.2	Doped SiC Sensor Films	24
		3.3.2.1 Doped SiC Film Structural Characteristics	26
		3.3.2.2 Doped Film Resistivity Characteristics	28
3.4	Cracking of the CVD Coatings		30
	3.4.1	CVD SiC on a Silicon Nitride Substrate	30

Preceding Page Blank

Table of Contents

Section			Page
		3.4.2 CVD Silicon Nitride on a SiC Substrate	31
	3.5	Conclusions	31
4.0	**Long/Short Wave Length Radiation Measurement**		32
	4.1	Introduction	32
	4.2	Work Scope	33
	4.3	Thermogage Emissometer	33
		4.3.1 Black Body Cavity	34
		4.3.2 Sample Specularity	34
		4.3.3 Sample Cooling	35
		4.3.4 Reflection from the Cup Lip	36
		4.3.5 Zirconia Oxygen Depletion	36
		4.3.6 Reflection Source	36
		4.3.7 Data Acquisition System	36
	4.4	Test Results	36
		4.4.1 Silicon Pyrometer Test Results	36
		4.4.2 Long Wavelength Test Results	38
		4.4.3 Short Wavelength Test Results	39
	4.5	Analysis	41
		4.5.1 Design Considerations	42
		4.5.1.1 Long Wavelength Design Considerations	42
		4.5.1.2 Long Wavelength Application	42
		4.5.1.3 Short Wavelength Design Considerations	42
		4.5.2 Reflected Energy	42
		4.5.3 Gas Emission and Absorption	43
	4.6	Conclusions	45
		4.6.1 Long Wavelength Radiation Measurements	45
		4.6.2 Short Wavelength Radiation Measurements	45
5.0	**References**		46

List of Illustrations

Figure		Page
1.	Phases 1 and 2 – MRC 8802 Sputtering Configuration.	3
2.	Phase 1 – Pt6%Rh Coating of 6 and 16 μm thickness on Alumina after 8 hours at 1371°C.	3
3.	Phase 1 – Pt30% Rh Coating of 7 and 10.5 μm thickness on Alumina after 8 hours at 1371°C.	4
4.	Phase 1 – Two Step Process. Initial thin Pt6%Rh coating (2.7 μm) on alumina after 1 hour at 1000°C in air.	4
5.	Phase 1 – Two Step Process. Initial thin Pt6%Rh coating (2.7 μm) on alumina after 1 hour at 1000°C in air.	4
6.	Phase 1 – Two Step Process. Second thick Pt6%Rh coating (total thickness 16 μm) on alumina after 4 hours at 1209°C in air.	5
7.	Phase 1 – Two Step Process. Second thick Pt6%Rh coating (total thickness 16 μm) on alumina after 4 hours at 1209°C in air.	5
8.	Phase 1 – Two Step Process. Second thick Pt6%Rh coating (total thickness 16 μm) on alumina after 4 hours at 1209°C in air.	6
9.	Phase 1 – Two Step Process. Second thick Pt6%Rh coating (total thickness 16 μm) on alumina after 4 hours at 1209°C in air.	6
10.	Phase 1 – Two Step Process. Second thick Pt6%Rh coating (total thickness 16 μm) on alumina after 4 hours at 1209°C in air. View of Broken Edge showing significant film porosity.	6
11.	Phase 1 – Two Step Process. Pt6%Rh film on alumina after an additional 8 hours at 1371°C.	6
12.	Phase 1 – Two Step Process. Pt6%Rh film on alumina after an additional 8 hours at 1371°C.	7
13.	Phase 2 – Pt6%Rh on Alumina Before Heating.	7
14.	Phase 2 – Pt6%Rh on Alumina after 1371°C for 8 hours.	7
15.	Phase 2 – Pt6%Rh on Mullite after 1371°C for 8 hours.	8
16.	Phase 2 – Pt30%Rh on Sapphire after 1371°C for 8 hours.	8
17.	Phase 2 – Cracks in Pt6%Rh on Mullite after 927°C Exposure.	9
18.	Phase 2 – Cracks in Pt6%Rh on Mullite after 927°C Exposure.	9
19.	Phase 3 – Coating Surface, As Sputtered.	11
20.	Phase 3 – Cross Section, As Sputtered.	11
21.	Phase 3 – Coating Surface: Anneal 2.	11
22.	Phase 3 – Cross Section: Anneal 2.	12
23.	Phase 3 – Coating Surface: Anneal 1.	12

List of Illustrations

Figure		Page
24.	Phase 3 – Cross Section: Anneal 1.	12
25.	Phase 3 – Coating Surface: Anneal 1) After 1600°C.	12
26.	Phase 3 – Coating Surface: Anneal 2) After 1600°C.	13
27.	Phase 3 – Coating Surface: No Anneal After 1200°C.	13
28.	Phase 3 – Coating Surface: Anneal 1 After 1300°C.	13
29.	Phase 3 – Coating Surface: Anneal 2 After 1300°C.	13
30.	Phase 3 – Coating Surface: No Anneal After 1200°C.	14
31.	Thin Film Thermocouple Configuration.	14
32.	Test Thermocouple Lead Attachment.	15
33.	Reference Thermocouple Attachment.	15
34.	Thermocouple Test Assembly.	16
35.	Installed Test Assembly.	16
36.	Thin Film Thermocouple Test.	17
37.	Thin Film Thermocouple Test.	18
38.	Concept Validation – Thin Film Application and Test Configuration.	22
39.	Thermoelectric Output versus Temperature for Two Forms of SiC versus Pt6%Rh.	23
40.	Concept Validation Coupon (Raytheon CVD SiC Substrate) Following Three Thermal Cycles to 954°C and One Cycle to 1093°C.	24
41.	Resistivity versus Temperature for CVD Silicon Nitride (17 μm thick) on a CVD SiC Substrate.	25
42.	CVD Silicon Nitride Film on a CVD SiC Substrate – As Deposited.	26
43.	CVD Silicon Nitride Film on a CVD SiC Substrate After Thermal Exposure to 1195°C for 4 hours; 1482°C for 8 hours; and 1593°C for 8 hours.	26
44.	"N" Doped SiC on Silicon Nitride Substrate showing Cracks in As Deposited Film.	27
45.	"N" Doped SiC on Silicon Nitride Substrate showing cracks in Film after 1371°C soak for 8 hours.	27
46.	"N" Doped SiC on an AIN Substrate As Deposited.	27
47.	"N" Doped SiC on an AIN Substrate As Deposited.	27
48.	"N" Doped SiC on an AIN Substrate after 1371°C for 8 hours.	28
49.	"P" Doped SiC Film on a Silicon Nitride Substrate As Deposited.	28
50.	"P" Doped SiC Film on a Silicon Nitride Substrate after 8 hours at 1371°C.	28
51.	"P" Doped SiC on AIN Substrate As Deposited.	29
52.	"P" Doped SiC on AIN Substrate after 8 hours at 1371°C.	29

List of Illustrations

Figure		Page
53.	"P" Doped SiC on CVD Substrate As Deposited.	29
54.	"P" Doped SiC on Silicon Nitride Substrate after 8 hours at 1371°C.	29
55.	Thermogage Emissometer Schematic.	34
56.	Normalized Silicon Detector Output versus Time.	35
57.	Globar Distribution.	37
58.	Detector Output versus Time Thermogage Emissometer for Several Detector-Wavelength Combinations with and without Globar (VF = 0.198) 6.7 mm thick Zirconia, 8% Yttria.	39
59.	Long Wavelength Pyrometer Schematic.	40
60.	Short Wavelength System Schematic.	40
61.	Normalized Optical Muiltichannel Analyzer Output versus Time.	41
62.	Effect of Reflected Energy – 1.0 μm.	43
63.	Effect of Reflected Energy – 8.65 μm.	44
64.	Effect of Reflected Energy – 0.4 μm.	44
65.	Effect of Gas Emission/Absorption versus Pressure.	45

List of Tables

Table		Page
1.	Phases 1 and 2 Platinum Rhodium Thermocouple Sputtering Process.	2
2.	Surface Roughness Measurements.	10
3.	Phase 3 Platinum Rhodium Thermocouple Sputtering Process.	10
4.	Time at Temperature.	16
5.	Summary of Thin Film Thermocouple Drift Data.	19
6.	Resistivity Measurements of "N" and "P" Doped CVD SiC at Room Temperature.	30
7.	Difference in Thermogage Radiance from Black Body.	34
8.	Emittance Measurements.	37

1.0 Introduction

This report describes the work performed by GE Aircraft Engines for NASA Lewis Research Center in support of "Sensors for Ceramic Components in Advanced Propulsion Systems" Program (NASA Contract NAS3–25140). The work effort of this program is organized under several major categories as follows:

- Task 1 – Survey of Sensor Concepts
- Task 2 – Analysis of Sensor Concepts
- Task 3 – Review and Report
- Task 4 – Sensor System Design and Test Plan Formulation
- Task 5 – Fabrication of Sensor Systems
- Task 6 – Performance of Tests and Analysis of Results.

The work conducted on Tasks 1 and 2 has been reported in NASA Contractor Report 180900. This report summarizes the work conducted for Tasks 4, 5, and 6.

The use of ceramic materials for coatings and hot section components of advanced aerospace propulsion systems offers many benefits compared with conventional metallic materials including lower density, higher operating temperature, and lower cost. In addition to these, the indirect benefit of reduced or eliminated cooling air requirements (typically necessary for hot section metallic parts) can result in significant increases in overall engine performance.

The tasks of developing ceramic materials suitable for use in advanced engines and then evaluating specific operating component hardware will require extensive testing of both materials and prototype hardware.

The purpose of the work described hereafter was to develop practical techniques for measurement of surface temperature on high temperature ceramic materials using methods suitable for real world testing of components and engines operating outside an artificially limited laboratory environment.

The approach has been to define the current state of the art in surface temperature measurement by means of a literature survey and by discussions with scientists active in this field. An assessment was made of the potential for adapting the various techniques for use with ceramic materials using the current types of testing typically required for development programs associated with advanced propulsion systems. The various techniques were ranked according to their potential and three were selected for further study, including design, fabrication, and evaluation of a prototype on selected ceramic materials.

In addition to surface temperature measurement, the literature survey included both strain and heat flux sensors. These were not fabricated into prototype sensors or evaluated for actual measurement performance.

The three surface temperature concepts selected for prototype fabrication and test were:

- Platinum rhodium alloy thin film thermocouple for use on high expansion or nonsilicon-based ceramic materials.
- Silicon carbide thin film thermocouple for use on low expansion or silicon-based ceramic materials.
- Long and short wavelength radiation pyrometers.

2.0 Platinum Rhodium Thin Film Thermocouple

There has been much interest in platinum rhodium alloy thin film thermocouples for application to metallic substrates.[1,2,3,4] Recently, work on applying these thermocouples to ceramic substrates has been initiated.[5,6] The purpose of this effort was to develop a technique for applying Type B thin film thermocouples to both alumina and mullite substrates using RF diode sputtering. The alloys of Type B thermocouples are platinum with 6% rhodium (Pt6%Rh) versus platinum with 30% rhodium (Pt30%Rh).

2.1 Coating Development – Phase 1

2.1.1 Test Plan

The intent of the initial phase of this effort was to manufacture a series of test coupons consisting of two thicknesses (8 and 12 μm) of Pt6%Rh and Pt30%Rh on both alumina and mullite substrates using oxygen-enhanced sputtering for the first several hundred angstroms to promote adhesion. The mullite substrates were not part of the original test matrix and were added later at NASA's request. The sputtering process parameters and substrates are defined in ***Table 1*** and the configuration of the sputtering machine is shown in ***Figure 1***.

These coupons were used to determine the upper temperature limit for the films by thermally soaking at temperatures of 1371°C and above. The coupons were evaluated for deterioration in adherence and film oxidation. The formation of a volatile oxide was anticipated to cause a reduction in film thickness as a function of time and temperature.

We intended to apply the platinum rhodium alloy films with both controlled heating and bias applied to the substrate. Controlled heating of the substrates turned out to be impractical due to the configuration of the sputtering system. Substrate bias control was incorporated but required changes to the sputtering system and some of the initial coupons were manufactured without bias voltage.

2.1.2 Initial Results

The configuration of the sputtering machine (MRC 8802) could not provide both substrate motion and perform a preliminary sputter etch to clean the substrate surface prior to coating application. Substrate motion improves the coating thickness uniformity across the substrate. To determine if the thickness variability would be acceptable with a stationary substrate it was decided to coat an alumina substrate with Pt6%Rh and measure the thickness of the coating as a function of

Table 1. Phases 1 and 2 Platinum Rhodium Thermocouple Sputtering Process.

Machine: MRC 8802	Process:
Alloys:	RF diode sputtering.
Platinum 6% Rhodium	With and without substrate bias.
Platinum 30% Rhodium	Substrates mounted above target due to the unbonded targets.
Targets: 15.2 cm diameter, unbonded	Sputter etch for 15 minutes before sputtering coating.
Substrate Materials:	Vacuum released and substrates repositioned between sputter etch and sputter coating.
Alumina: MRC, Superstrate™ 99.6% Alumina, tape cast, as fired finish (7–10 microinches).	First 0.1 μm reactive sputtered with 20% oxygen.
Mullite: Coors, 60% Alumina, 40% Silica, extruded, as fired finish (50–60 microinches).	No external substrate heating.
Sapphire: Union Carbide, Part No. 6290, sapphire flats (6–9 microinches), 0.5 mm thick.	A film thickness of 8 and 12 μm was the goal.

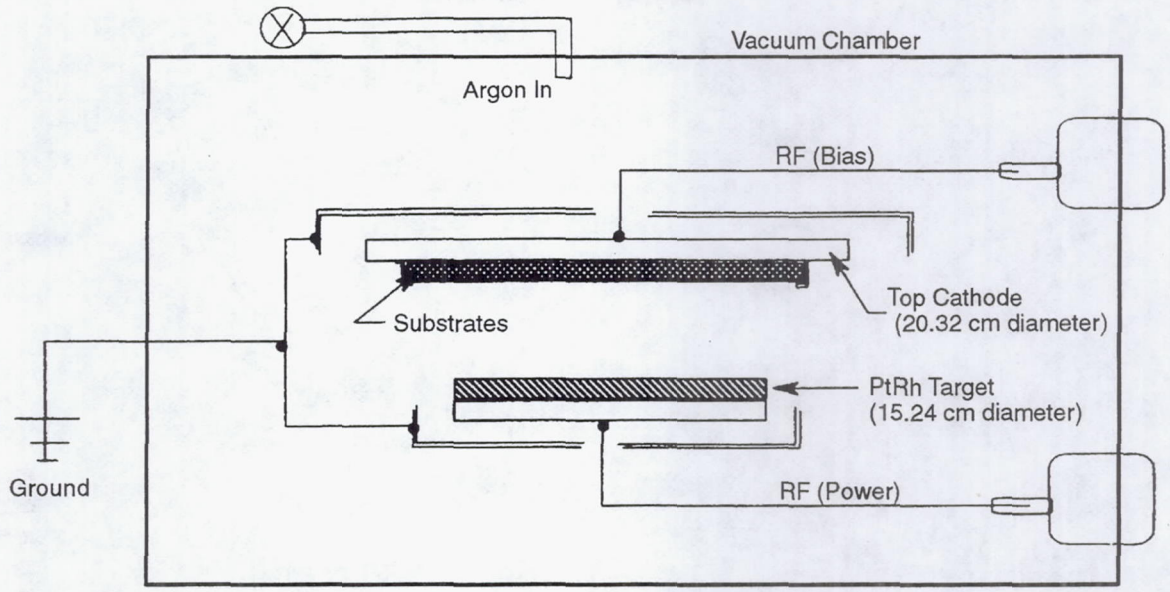

Figure 1. Phases 1 and 2 – MRC 8802 Sputtering Configuration.

substrate position relative to the sputtering target. Following a series of preliminary sputtering runs to establish the process parameters, the thickness variation coupon was coated. The coating thickness of a broken cross section at the center of the 11.45 cm long substrate and another near its outer end was measured by scanning electron microscope (SEM) to be 5.65 and 4.8 μm, respectively. This variability was deemed to be acceptable.

To evaluate the effects of heating on film adhesion, a pair of Pt6%Rh films in two thicknesses (6 and 16 μm) and a pair of Pt30%Rh films in two thicknesses (7 and 10.5 μm) were produced (all on alumina substrates). After an 8-hour soak at 1371°C (in air), all four showed some signs of film distress (***Figures 2*** and ***3***). Particularly severe localized separation occurred on the 16 μm Pt6%Rh film. The appearance of the films on all four of these coupons indicated that outgassing the substrate material (99.8% alumina) may have contributed to film distress.

To evaluate if outgassing was the source of the poor adhesion, an alumina coupon was baked at 1371°C to allow outgassing of impurities and then coated with Pt6%Rh. This coupon experienced major film loss during the first thermal cycle (1190°C, 3 hours). Although this may have been caused by sputter process variability, there was not enough time nor resources to conduct a more detailed study related to the effects of prebaking substrates to minimize effects of outgassing on film adherence. Discussions with David Skelly, GE Corporate Research and Development Center (GE-CRD), indicated that using sapphire substrates would be a better plan. There were concerns that prebaking could cause impurities in the MRC Superstrate™ alumina

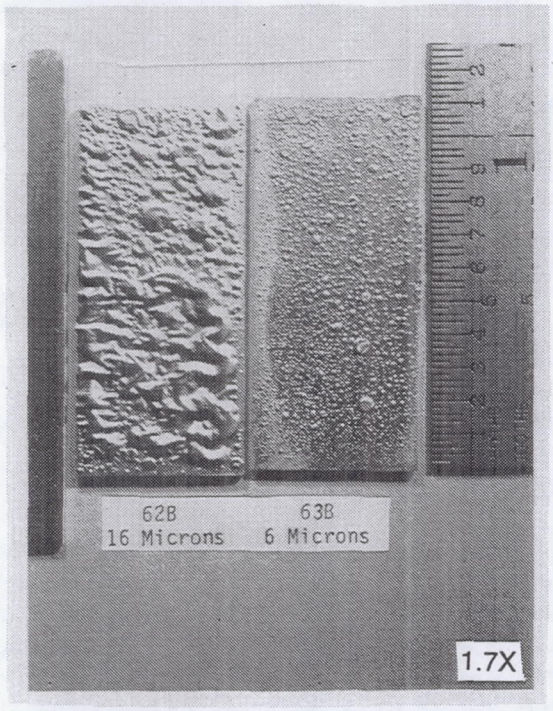

Figure 2. Phase 1 – Pt6%Rh Coating of 6 and 16 μm thickness on Alumina after 8 hours at 1371°C. *(1.7X)*

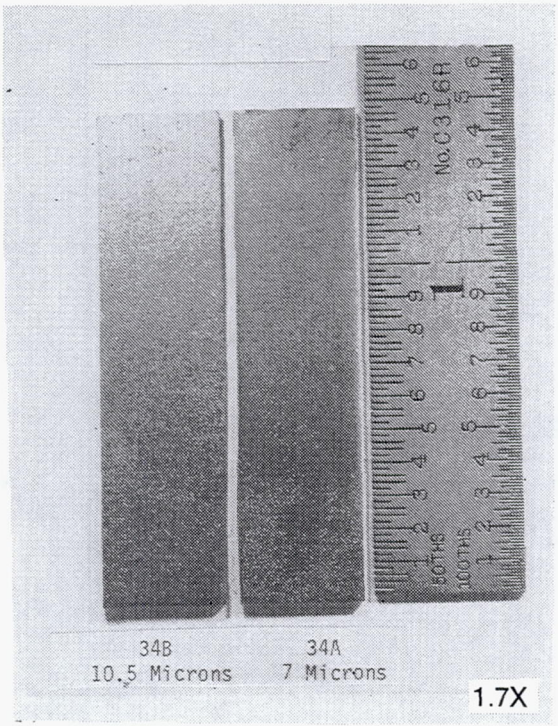

Figure 3. Phase 1 – Pt30% Rh Coating of 7 and 10.5 μm thickness on Alumina after 8 hours at 1371°C. *(1.7X)*

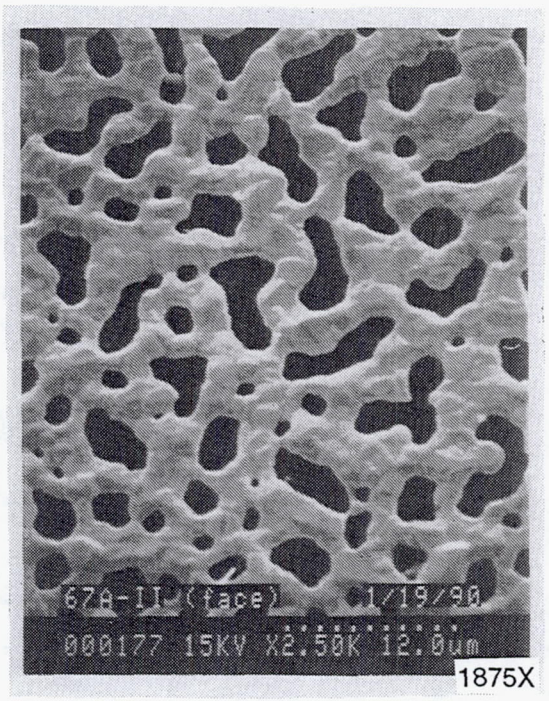

Figure 4. Phase 1 – Two Step Process. *Initial thin Pt6%Rh coating (2.7 μm) on alumina after 1 hour at 1000°C in air. (1875X)*

substrates to become concentrated at the surface. Since the major impurity in high purity alumina is silica, which forms a low melting point eutectic with platinum, sapphire (with inherently low levels of silica) substrates were chosen to help determine if some physical/chemical characteristics of the high purity alumina substrates were causing adherence problems.

Sapphire substrates were obtained and tested as described below as part of Phase 2 development. Platinum rhodium alloy film adherence on sapphire was far worse than any other substrate material. A preliminary conclusion was reached that internal impurities were not a probable cause for poor adherence.

2.1.3 Two Step Process

Another approach to improving film adherence on high purity alumina substrates was evaluated. This consisted of applying a very thin Pt6%Rh film (less than 1 μm) followed by a 1000°C bake in air for an hour prior to sputtering additional Pt6%Rh for a total of 15 μm. ***Figures 4*** and *5* show the film face of a coupon that has the thin Pt6%Rh film followed by the 1000°C bake. Grain growth and agglomeration of the film (Area b) surrounding islands of voids (Area a) are visible on these

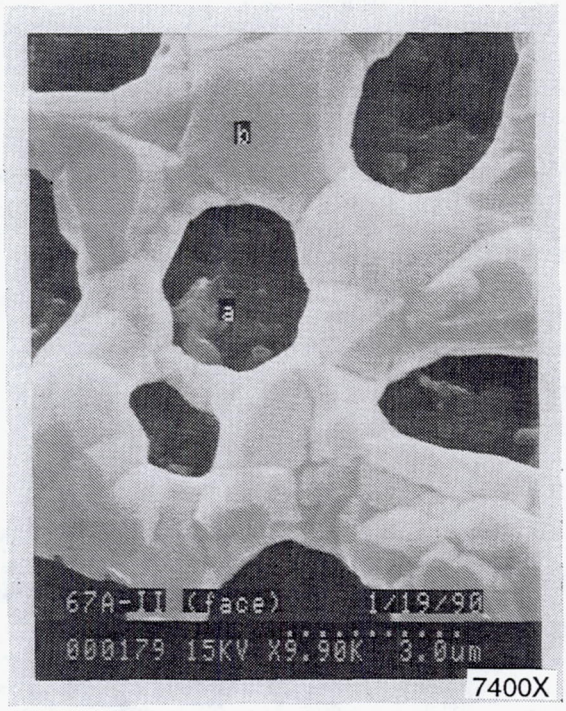

Figure 5. Phase 1 – Two Step Process. *Initial thin Pt6%Rh coating (2.7 μm) on alumina after 1 hour at 1000°C in air. (7400X)*

SEM photographs. After the 1000°C bake, the maximum film thickness had increased to 2.7 μm.

Figures 6 through ***9*** are SEM photographs of the coupon surface after the second, thicker layer (13.3 μm) of Pt6%Rh has been applied over the thin, baked film and the composite coating was baked for 4 hours at 1209°C. The intended temperature was 1371°C but, because the coupon was located within a closed end alumina tube to isolate it from possible contaminants in the oven, the coupon temperature was limited to 1209°C. ***Figure 10*** is a 2250X SEM photograph of the broken edge of the coupon. It shows the two layer alloy film with significant porosity in the top (13.3 μm) layer and what appears to be debonding between the lower (2.7 μm) film and the alumina substrate.

A direct comparison between single step (***Figure 2***) and two step (***Figure 6***) films of the same thickness (16 μm) shows significantly less distress in the two step film. In order to determine whether this was due to superior film adhesion characteristics of the two-step process or to the lower soak temperature (1209° versus 1371°C), a small piece of the two-step coupon was soaked at 1371°C for 8 hours. ***Figures 11*** (7X) and ***12*** (40X) show the face of this coupon after the 1371°C soak. Although there was significant bubbling of the two-step film after the 1371°C soak, it exhibited better adhesion than the

Figure 7. Phase 1 – Two Step Process. *Second thick Pt6%Rh coating (total thickness 16 μm) on alumina after 4 hours at 1209°C in air. (750X)*

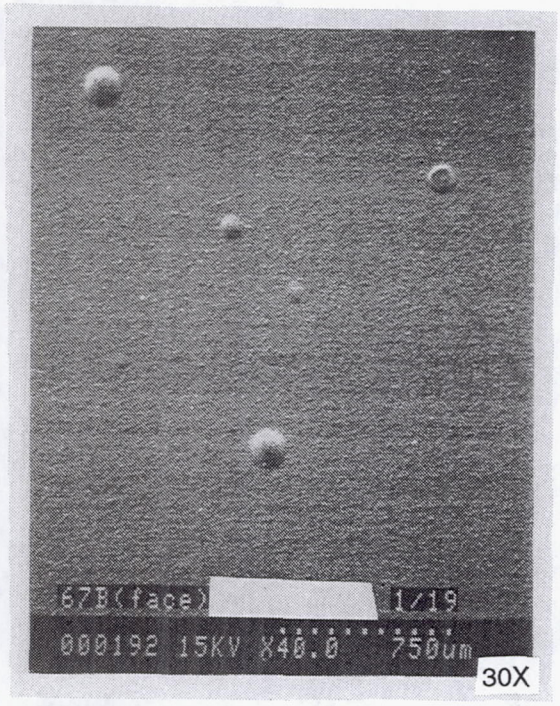

Figure 6. Phase 1 – Two Step Process. *Second thick Pt6%Rh coating (total thickness 16 μm) on alumina after 4 hours at 1209°C in air. (30X)*

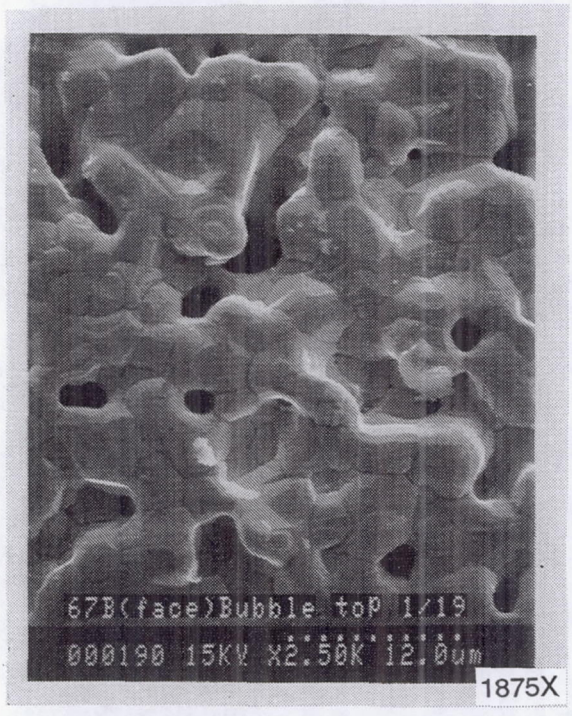

Figure 8. Phase 1 – Two Step Process. *Second thick Pt6%Rh coating (total thickness 16 μm) on alumina after 4 hours at 1209°C in air. (1875X)*

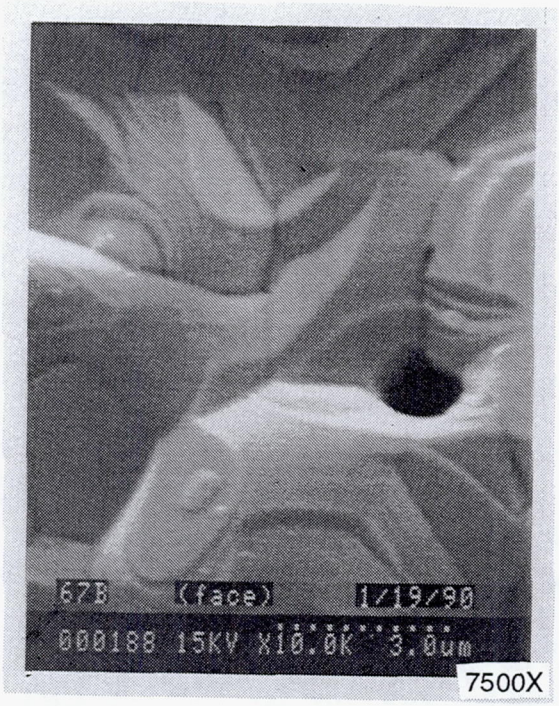

Figure 9. Phase 1 – Two Step Process. *Second thick Pt6%Rh coating (total thickness 16 μm) on alumina after 4 hours at 1209°C in air. (7500X)*

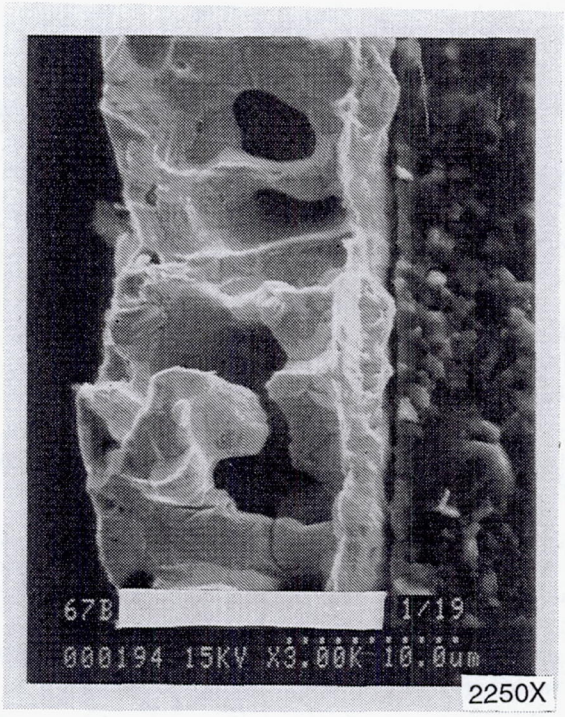

Figure 10. Phase 1 – Two Step Process. *Second thick Pt6%Rh coating (total thickness 16 μm) on alumina after 4 hours at 1209°C in air. View of Broken Edge showing significant film porosity. (2250X)*

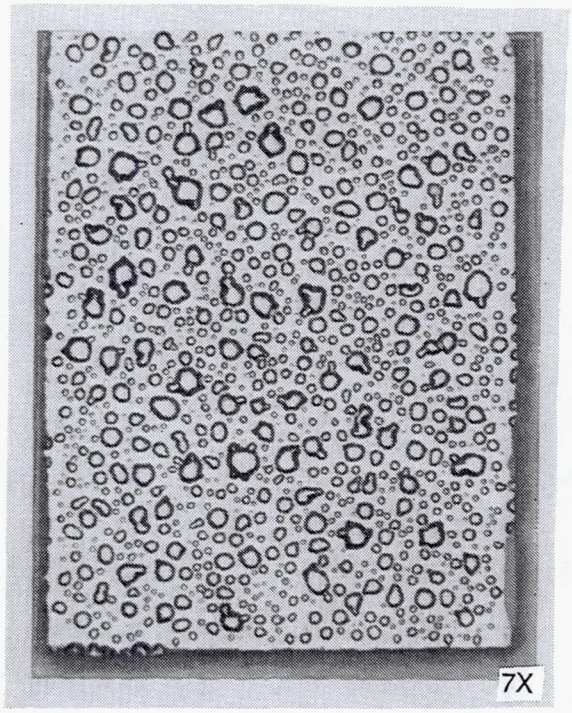

Figure 11. Phase 1 – Two Step Process. *Pt6%Rh film on alumina after an additional 8 hours at 1371°C. (7X)*

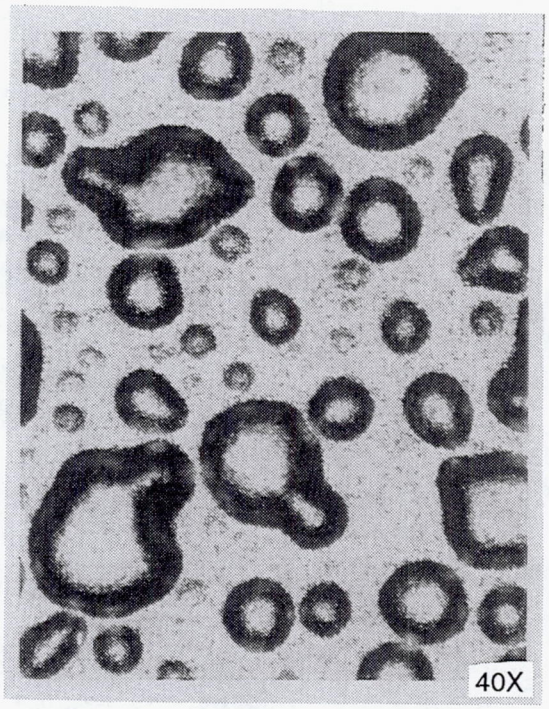

Figure 12. Phase 1 – Two Step Process. *Pt6%Rh film on alumina after an additional 8 hours at 1371°C. (40X)*

16 μm thick single-step film shown in ***Figure 2***. This comparison is the basis for the conclusion that the two-step film application process is superior to the single-step process. It is based on the assumption that the process variables were the same for both coupons. This assumption is tenuous because of the many variables associated with the thin film application process.

2.2 Coating Development – Phase 2

The second phase of coupon work was intended to evaluate the adherence problems encountered during the first phase of development. A test plan was formulated that included the application of platinum rhodium alloy films to sapphire, alumina, and mullite substrates. The two-step process and the effectiveness of alumina and hafnia top coats in extending the upper temperature limit were to be evaluated.

In the first runs of the second phase of coupons, Pt6%Rh and Pt30%Rh films were applied to 1371°C prebaked alumina, mullite, and sapphire substrates to determine if impurities in the substrate materials were interfering with adherence and, if so, to find out if they could be eliminated with a prebake cycle.

Prior to thermal exposure, a visual inspection of the Pt6%Rh films showed satisfactory adherence on the mullite and sapphire substrates and poor adherence on the alumina substrates.

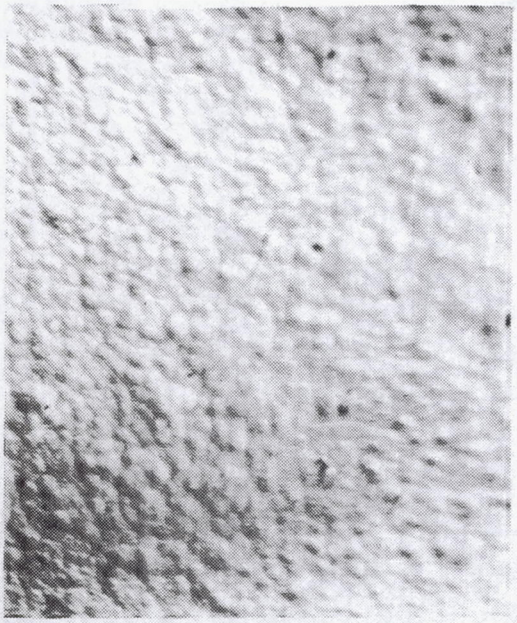

Figure 13. Phase 2 – Pt6%Rh on Alumina Before Heating. *(600X)*

2.2.1 1371°C Heat Treat

A group of three of each film alloy on both alumina and mullite substrates plus one of each film alloy on sapphire substrates were thermally soaked at 1371°C for 8 hours in air with no preliminary stabilization or annealing cycles. Actual film thicknesses were measured to be between 9.5 and 15.6 μm on six separate cross sections.

One piece of each coated substrate was positioned on an alumina block (5.1 x 15.24 x 1.27 cm) but isolated from direct contact with the block by a piece of zirconia felt. Two such assemblies were loaded in an oven and slowly heated to 1371°C.

Both alloy films showed severe distress on alumina and sapphire substrates with only minor changes on the mullite substrates. ***Figures 13*** and ***14*** show Pt6%Rh coating on alumina before and after heating. ***Figure 15*** shows a Pt6%Rh coating on mullite after heating. ***Figure 16*** shows a Pt30%Rh coating on sapphire after heating.

This would suggest that substrate outgassing is probably not responsible for film bubbling and adherence loss on the 99.6% alumina because it was more severe on the sapphire substrates which had inherently low internal impurity levels. The improved adhesion of both platinum alloys on mullite is probably due to chemical bonding or increased surface roughness (compared with both the alumina and sapphire).

Figure 14. Phase 2 – Pt6%Rh on Alumina after 1371°C for 8 hours. *(40X)*

40X

Figure 15. Phase 2 – Pt6%Rh on Mullite after 1371°C for 8 hours. *(40X)*

5X

Figure 16. Phase 2 – Pt30%Rh on Sapphire after 1371°C for 8 hours. *(5X)*

In an attempt to gain understanding of the causes for the film distress, samples of each Pt6%Rh and Pt30%Rh on alumina, mullite, and sapphire were incrementally soaked for nominally 4 hours each at 538°, 704°, 816°, 927°, and 1010°C in air.

The 538°C soak produced no changes in film appearance except for an almost total debonding of the Pt6%Rh film on the sapphire substrate.

- Some very localized and minor bubbling of films on the alumina substrates.
- Severe wrinkling of the Pt30%Rh film on sapphire.

After the 704°C soak, no additional changes were observed.

After the 816°C soak, the Pt6%Rh films were noticeably darker than the Pt30%Rh films. There were no additional changes in bubbling or adherence.

The 927°C soak caused the following changes to the coatings:

- Cracks formed over the entire surface of both alloys on mullite substrates. The alloy films were typically raised somewhat at the crack edges. The cracks were present in both alloys but more prominent for the Pt6%Rh films. The cracks could not be seen on the Pt30%Rh films below 500X. ***Figures 17*** and ***18*** show cracks in the films which are typical of the entire surface.
- Significant lightening in color for the Pt30%Rh films on alumina.

The 1010°C soak did not result in any additional changes of significance.

The cracks in the platinum rhodium alloy films on the mullite coupons were not anticipated because previous tests of sections from the same coupons did not show cracks following 1371°C exposure for 8 hours. Additional thermal cycles associated with the lower temperature tests may have caused the cracks.

2.2.2 Surface Roughness Measurements

Surface roughness measurements of the three substrate materials were made to evaluate the possibility that adherence at elevated temperatures was enhanced by surface roughness.

Measurements were made using a stylus type instrument manufactured by Gould Instruments. The results are shown in ***Table 2***. This data is consistent with the theory that increased surface roughness improves adhesion. Additional investigation is required.

2.2.3 Auger Analysis

An Auger analysis was conducted on both the Pt6%Rh and Pt30%Rh films as sputtered and after the 1371°C 8-hour thermal exposure to determine if there were any

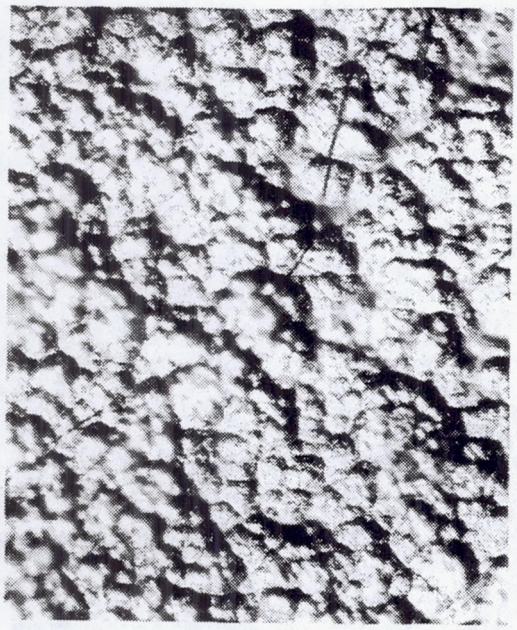

20X

Figure 17. Phase 2 – Cracks in Pt6%Rh on Mullite after 927°C Exposure. *(20X)*

300X

Figure 18. Phase 2 – Cracks in Pt6%Rh on Mullite after 927°C Exposure. *(300X)*

Table 2. Surface Roughness Measurements.

Substrate	µm	Film Condition after 1371°C Soak
Mullite	2000 – 2400	Some deterioration – but usable
Alumina	270 – 390	Badly wrinkled/distorted – unusable
Sapphire	130 – 350	Totally separated – unusable

changes in the alloy constituents near the outer surface caused by selective oxidation/evaporation of the constituents. Unconfirmed variability in the platinum/rhodium (ratio) had been indicated during Energy Dispersive X-ray (EDX) analysis of previous samples. The Auger work was done by Perkin Elmer at their Physical Electronics Laboratory in Edison, New Jersey, using a Model 660 Scanning Auger Microprobe, and is much more precise than the EDX analysis.

Plots of alloy constituents averaged over a 150 x 200 µm rectangular cross section area at 300 Angstrom increments from the outer surface to depths of 22,500 angstroms for the Pt6%Rh and 9,000 angstroms for the Pt30%Rh showed the following:

- Consistent platinum rhodium ratio beyond a depth of 1500 angstroms for both the heated and unheated samples.
- Absolute platinum rhodium ratios consistent with the desired 6% and 30% levels for both heated and unheated samples.
- No evidence of silicon reacting or diffusing up from the substrate. Platinum silicide formation had been a concern because of its low melting point.

2.2.4 Conclusions

Following disappointing results with regard to identifying the source of adherence degradation caused by thermal exposure on alumina, mullite, and sapphire at 1371°C, alternatives were considered. The original plan of evaluating the two-step coating process and applying alumina and hafnia top coats was changed. Instead, it was decided to revise the process and initiate a third phase of coupon evaluation to determine the cause of the adherence problem.

2.3 Coating Development – Phase 3

Two major changes were made to the sputtering process for Phase 3; bonded targets and reduced film thickness. The previous work was conducted with unbonded sputtering targets that have a greater probability of producing nonuniform coatings. These were replaced with bonded targets that also eliminated the need to reposition the substrate coupon between the sputter etch (surface cleaning) and the film deposition operations. In addition, the thickness of the coating was reduced from 10 to 5 μm to improve adhesion. The process used for the current work is described in ***Table 3***.

During the preparation for this phase of the program, a violent transformation from amorphous to granular structure was observed in the previously applied coatings when they were subjected to approximately 1000°C. Coincidentally, the heat treatment of the first coating layer for the two-step process was conducted at 1000°C. The first step in analyzing the adhesion problem was the evaluation of the effect of annealing the thin films after deposition and understanding this transformation and its effect on adhesion.

2.3.1 Post-Process Anneal

Coupons were fabricated to evaluate the effects of post-process annealing, various substrates, and substrate preparation. Platinum 6% rhodium was chosen as the deposition material. Evaluation of the coupon run was begun with films deposited on alumina (MRC Superstrate™) to determine the effect of the anneal and the maximum functional temperature of the coating. The two anneals were:

1. 500° to 900°C in 100°C increments for 4 hours at each temperature, then 5 hours at 1000°C
2. 1000°C for 22 hours.

After the anneal and after each temperature step, the surface and cross section (edge broken before heating) were examined using an optical microscope from 8 to 1000 power. The following observations were made from this test:

- The coatings as deposited were amorphous and smooth with no visible porosity (***Figures 19*** and ***20***).
- During the 500° to 900°C phase of Anneal 1, there was no visible change in the coating structure.
- The transformation from amorphous to granular structure occurs in the coating at 1000°C and above. The samples that had Anneal 1 exhibited a finer grain structure and less porosity in the cross section than Anneal 2. This is shown in ***Figures 21*** to ***24***.
- The samples were tested at 1100°, 1200°, 1300°, 1400°, 1500°, 1600°, and 1650°C (maximum for furnace) for 4 hours at each temperature. Samples with both anneals were still adherent upon completion of the 1650°C test point (***Figures 25*** and ***26***). Some small (20 μm) bubbles over 50% of the surface were observed on one sample with Anneal 1 after the 1100°C point. These were the only bubbles observed during the testing and they remained the same size after the subsequent points.

Table 3. Phase 3 Platinum Rhodium Thermocouple Sputtering Process.

Machine: MRC 8802 Alloys: Platinum 6% Rhodium Platinum 30% Rhodium Targets: 15.2 cm diameter, bonded Substrate Materials Alumina: MRC, Superstrate™ 99.6% Alumina, tape cast, as fired finish (7–10 microinches) Mullite: Coors, 60% Alumina, 40% Silica, extruded, as fired finish (50–60 microinches) Sapphire: Union Carbide, Part No. 6290, sapphire flats (6–9 microinches), 0.5 mm thick	Process: RF diode sputtering No substrate bias Target mounted above substrate (normal configuration) Sputter etch for 15 minutes before sputtering coating Vacuum maintained between sputter etch and sputter coating First 0.1 μm reactive sputtered with 20% oxygen No external substrate heating Film thickness of 5 μm

Figure 19. Phase 3 – Coating Surface, As Sputtered. *(600X)*

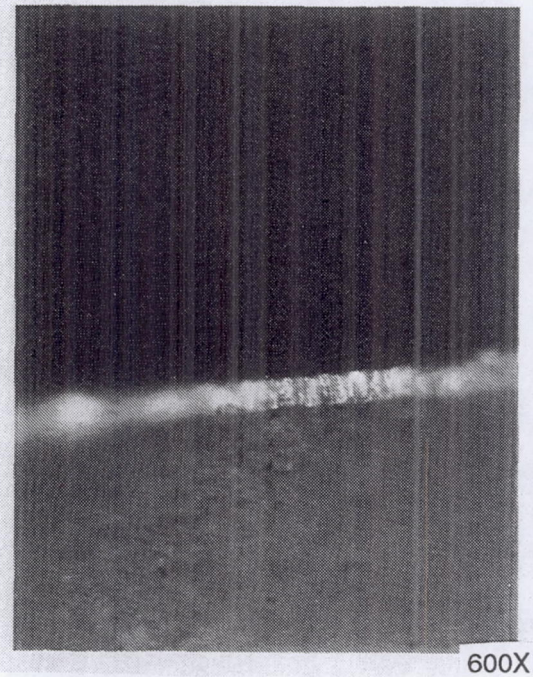

Figure 20. Phase 3 – Cross Section, As Sputtered. *(600X)*

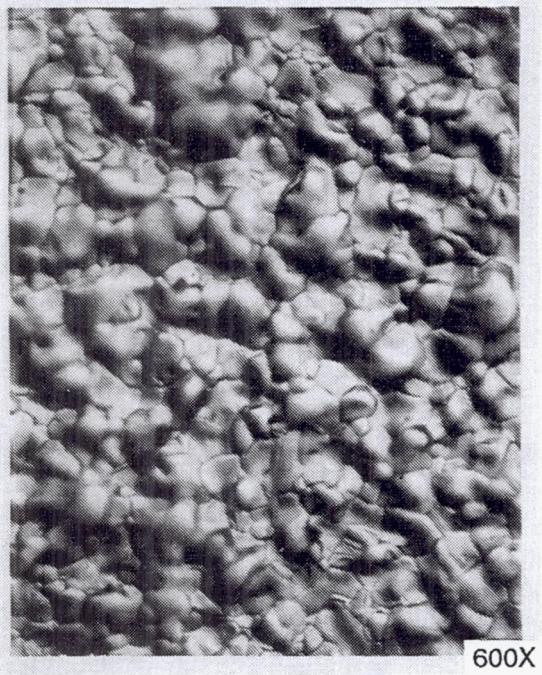

Figure 21. Phase 3 – Coating Surface: Anneal 2. *(600X)*

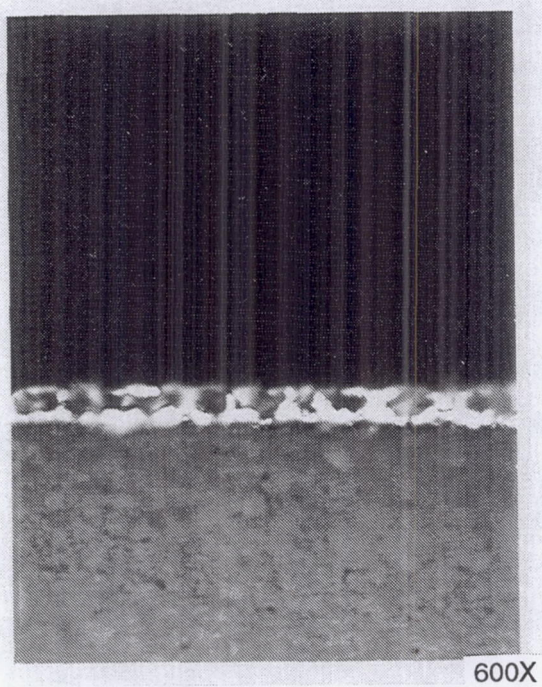

Figure 22. Phase 3 – Cross Section: Anneal 2. *(600X)*

Figure 23. Phase 3 – Coating Surface: Anneal 1. *(600X)*

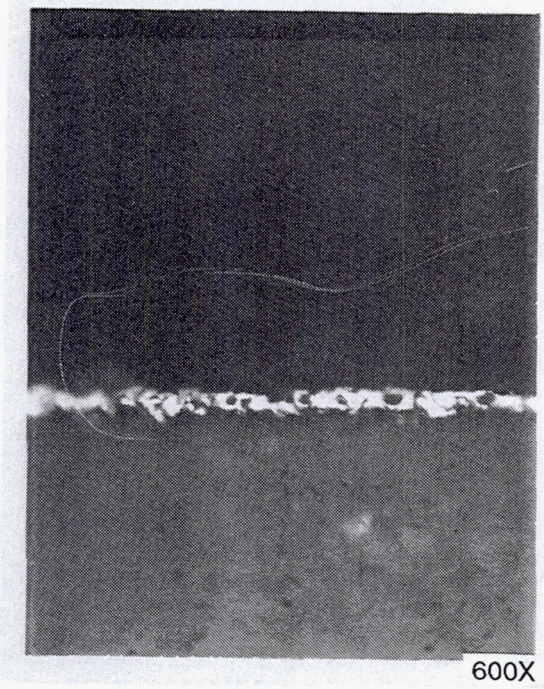

Figure 24. Phase 3 – Cross Section: Anneal 1. *(600X)*

Figure 25. Phase 3 – Coating Surface: Anneal 1 After 1600°C. *(600X)*

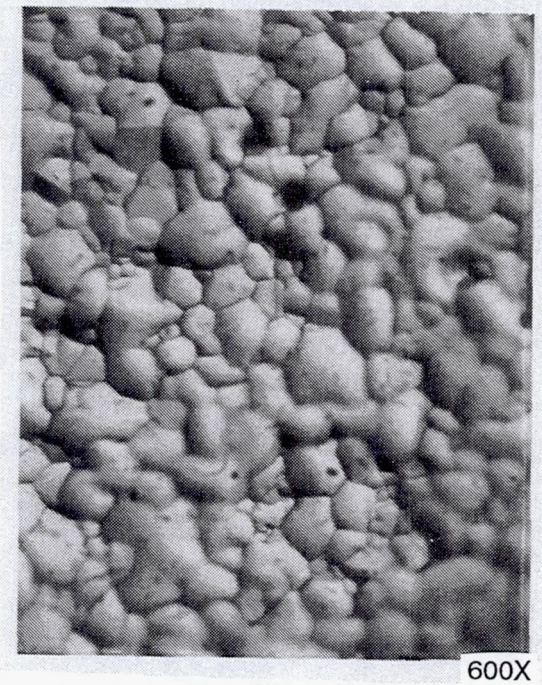

Figure 26. Phase 3 – Coating Surface: Anneal 2 After 1600°C. *(600X)*

- One sample with no previous heat treat was included with the other test specimens at the 1200°C test point. This sample exhibited large bubbles (32 to 450 μm) over the entire surface (***Figure 27***) showing the importance of the anneal.
- Small pores (3 μm) were observed in the coating surface after the 1000°C exposure in both anneals that became larger (6 μm) and better defined as the temperature testing continued. By back illumination of the samples the pores were shown to penetrate through the coating (***Figures 28*** and ***29***). An "as sputtered" sample was then examined that showed no pores or light penetration. Finally, the sample that bubbled at the 1200°C point was examined in the area between the bubbles and showed very few pores with no light penetrating (***Figure 30***).

The following conclusions can be drawn from this test:

- The coating exceeded all expectations for maximum operating temperature.
- The anneal is critical to obtain coatings that do not bubble.
- Pore formation may be the mechanism that prevented bubbling during this test.

2.4 Thermocouple Fabrication and Testing

Thin film thermocouples were fabricated on four MRC Superstrate™ alumina and three Coors mullite substrates using the same process parameters as the Phase 3 coating development. The thin film thermocouple circuit was formed by using physical masks (made from alumina or mullite substrates) to limit the coatings to the desired areas. The configuration of the thin film thermocouple is shown in ***Figure 31***.

Due to funding constraints, only a single sensor could be tested. One thermocouple on alumina was selected.

2.4.1 Test Setup

Based on the results of previous work, the entire coupon was first annealed for 23 hours at 975°C. After the anneal, bubbles averaging 0.1 mm were observed over 20% of the Pt6%Rh coating surface. The bubbles remained the same size and did not interfere with the subsequent testing.

The electrical connection to the sample was made by attaching both copper and constantan wires to each leg of the test thermocouple by means of an electrically conductive adhesive. The test thermocouple's output

Figure 27. Phase 3 – Coating Surface: No Anneal After 1200°C. *(6X)*

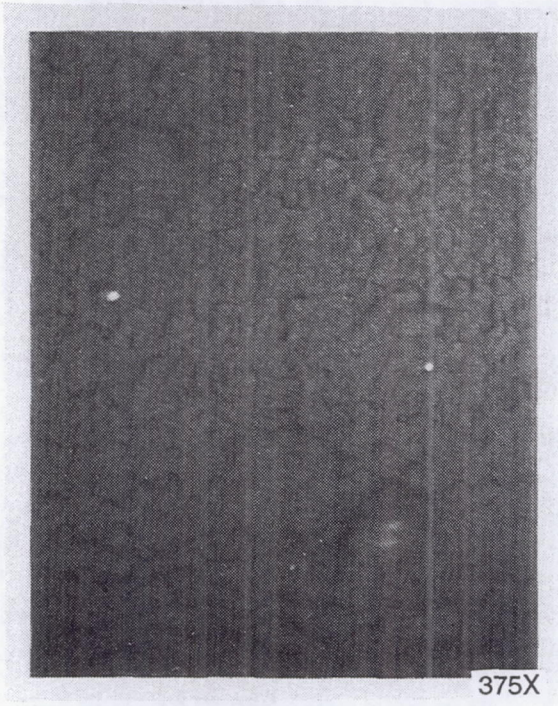

Figure 28. Phase 3 – Coating Surface: Anneal 1 After 1300°C. *(375X) Back Illumination*

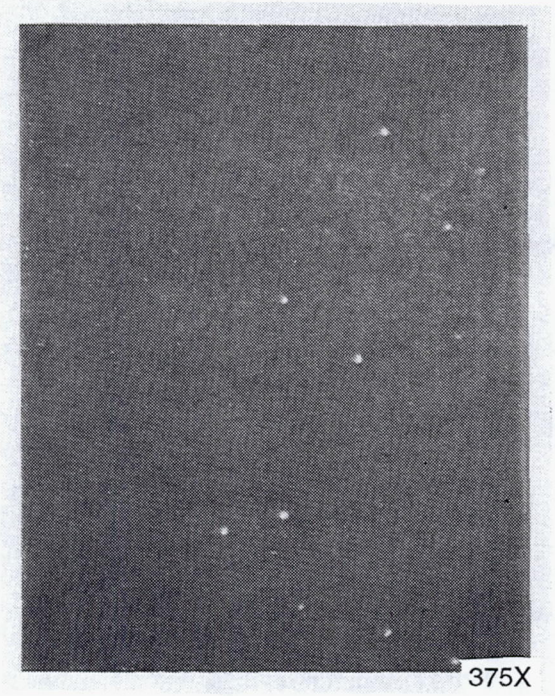

Figure 29. Phase 3 – Coating Surface: Anneal 2 After 1300°C. *(375X) Back Illumination*

Figure 30. Phase 3 – Coating Surface: No Anneal After 1200°C. *(375X) Back Illumination*

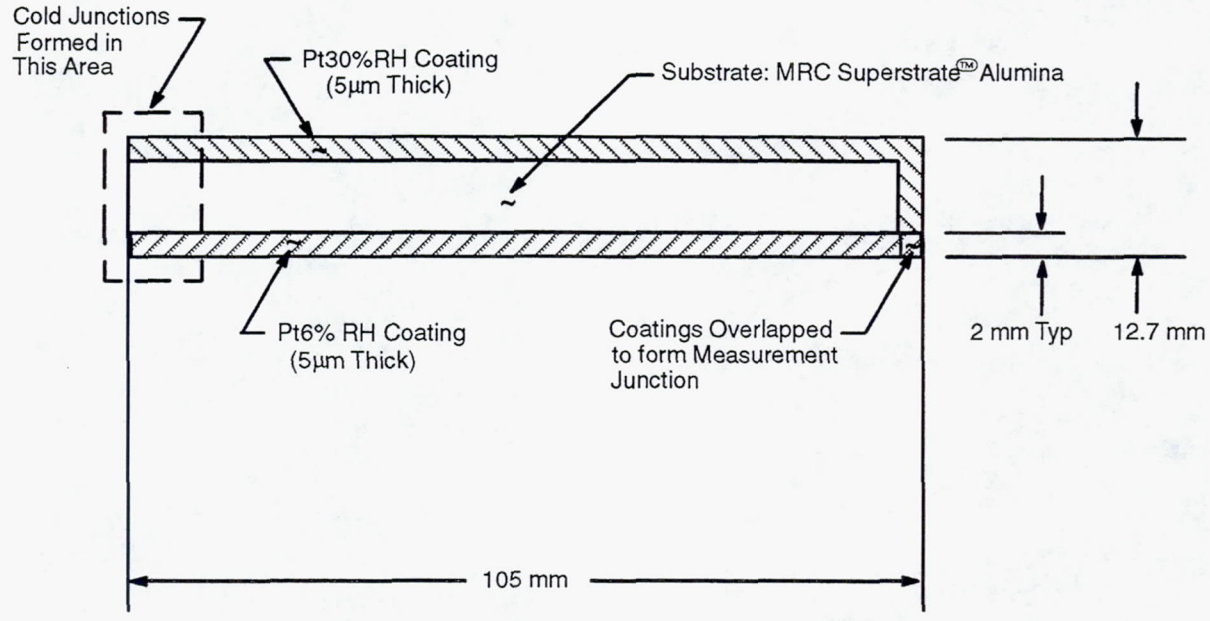

Figure 31. Thin Film Thermocouple Configuration.

was measured across the two copper leads. This formed the cold junctions for the test thermocouple. The temperature of each cold junction was measured using the copper-constantan thermocouple formed at the junction. The lead attachment is shown in ***Figure 32***.

The temperature fluctuations of the cold junctions were not anticipated to cause a significant variation in the test thermocouple's output. Thermocouple temperature versus electromotive force tables are based on a cold junction at 0°C, but a Type B thermocouple has very low sensitivity below 100°C. For example, the error caused by a 70°C cold junction would be only 1°C with the measurement junction at 1200°C.

A 1 mm diameter platinum sheathed, magnesium oxide insulated Type B thermocouple with a capped ungrounded junction was used as the temperature reference. The manufacturer's specified accuracy of the reference thermocouple was ± 1%. It was attached to the back of the test coupon opposite the measurement junction using ceramic cement. It was secured along its length using platinum wire wrapped around the substrate. The thermocouple attachment is shown in ***Figure 33***.

A test fixture was designed to support the sample and provide cooling air to the reference junctions. The test sensor was secured in the fixture using two set screws. Alumina shims were used to electrically isolate the sensor from the fixture. The sensor's penetration into the fixture was sealed with ceramic cement to prevent air leakage into the oven. The completed assembly is shown in ***Figure 34***.

The test fixture assembly was mounted in an oven through an access port in the top of the oven. The sensor was mounted vertically to minimize the gravity induced stress on the test coupon. The face of the fixture was located 15 mm above the inner wall of the oven. The area around the fixture was packed in a fibrous ceramic material to be flush with the oven wall. The installed assembly at the completion of testing is shown in ***Figure 35***.

2.4.2 Test Results

In order to obtain the most information from a single sensor, the sensor was exposed to increasing temperature in steps to the upper limit of the oven (1600°C). The sensor was held at a given temperature until the drift rate appeared to be relatively constant. Upon completion of the step test, testing was continued until sensor failure. In this way, calibration, drift rate, maximum operating temperature, and endurance data were obtained from a single sensor.

The test data is shown in ***Figures 36*** and ***37***. The reference thermocouple temperature, the thin film sensor deviation (reference minus thin film), and average cold junction temperature are plotted versus time. ***Figure 36*** shows the step test through 1600°C and

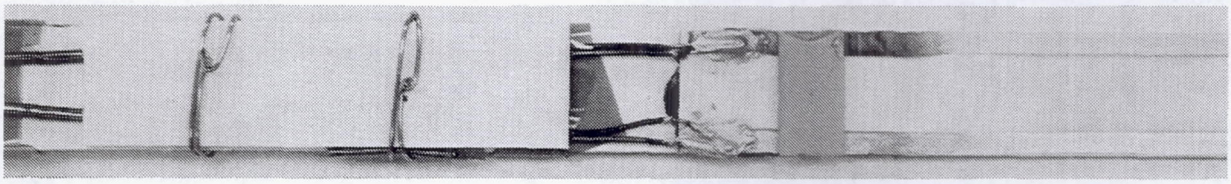

Figure 32. Test Thermocouple Lead Attachment.

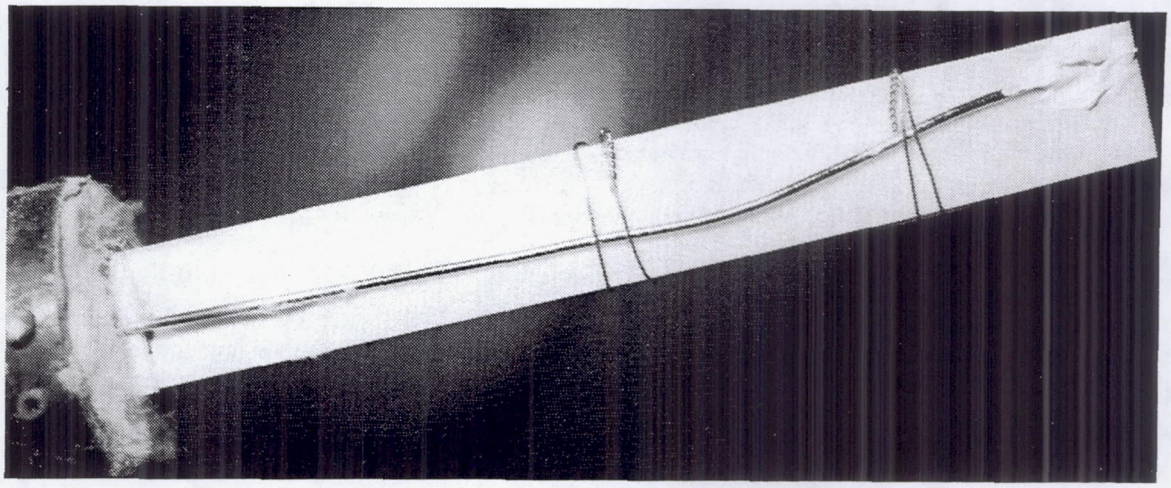

Figure 33. Reference Thermocouple Attachment.

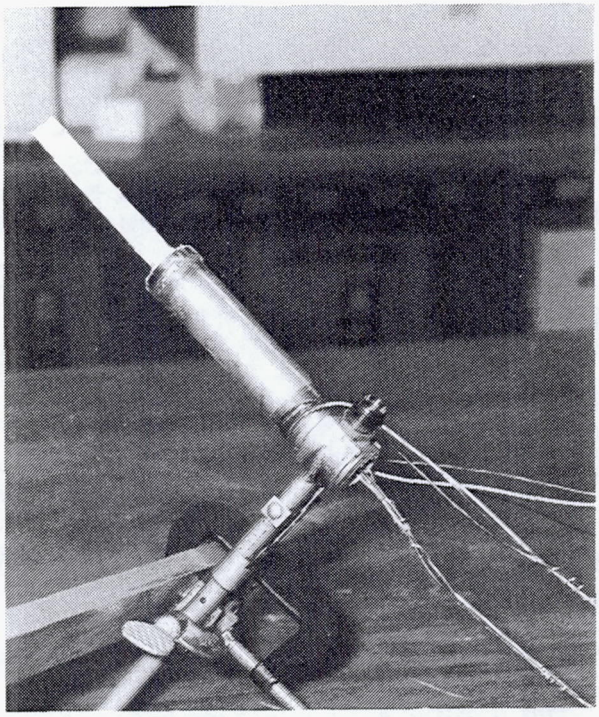

Figure 34. Thermocouple Test Assembly.

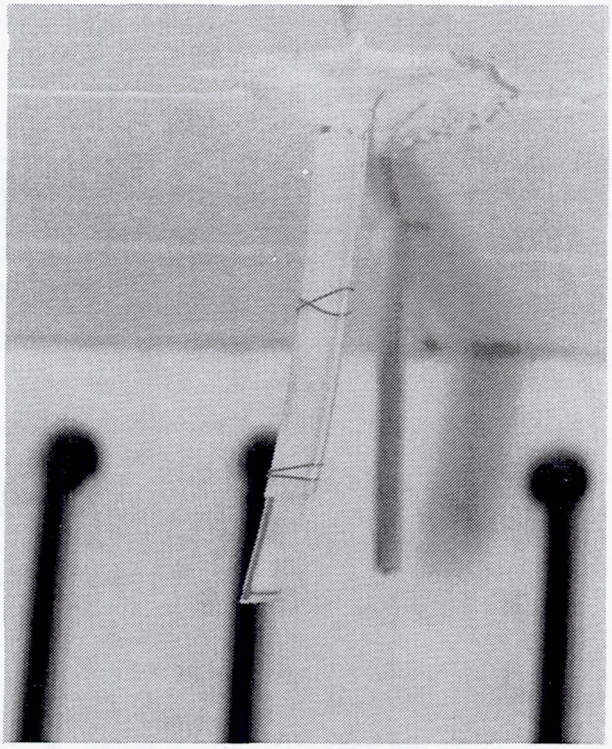

Figure 35. Installed Test Assembly.

Figure 37 shows the continued testing through the failure of the thin film thermocouple.

During the step test, the cooling airflow to the cold junctions varied due to changes in the supply pressure. The cold junction temperature varied as expected with the flow fluctuations (***Figure 36***). However, the variation in the thin film sensor deviation was much larger than could be explained by the effect of the cold junction variations on the thin film sensor output. As part of the subsequent testing (104 to 112 hours into the test) the effect of cooling flow was evaluated. Surprisingly, it was determined that the reference thermocouple was sensitive to variations in cooling flow. The only explanation is that this effect is caused by conduction along the length of the thermocouple. Funding did not permit further evaluation of this effect.

2.4.2.1 Thermocouple Endurance

The sensor performed well through the maximum test temperature of 1600°C (oven maximum). The eventual failure of the thin film thermocouple was caused by the complete oxidation of the Pt30%Rh leg. The total time at each of the various test temperatures is shown in ***Table 4***.

Table 4. Time at Temperature.

Temperature (°C)	Time (hours)
750	3
1000	2
1200	44
1300	4
1400	34
1500	14
1600	4
Total	105

2.4.2.2 Thermocouple Calibration

The thin film thermocouple agreed with the reference thermocouple within ± 4% during the entire test. The effect of the cooling flow on the reference thermocouple would tend to reduce this difference between the reference and thin film thermocouples. The effect of the cooling flow on the reference thermocouple is estimated to be less than 2%.

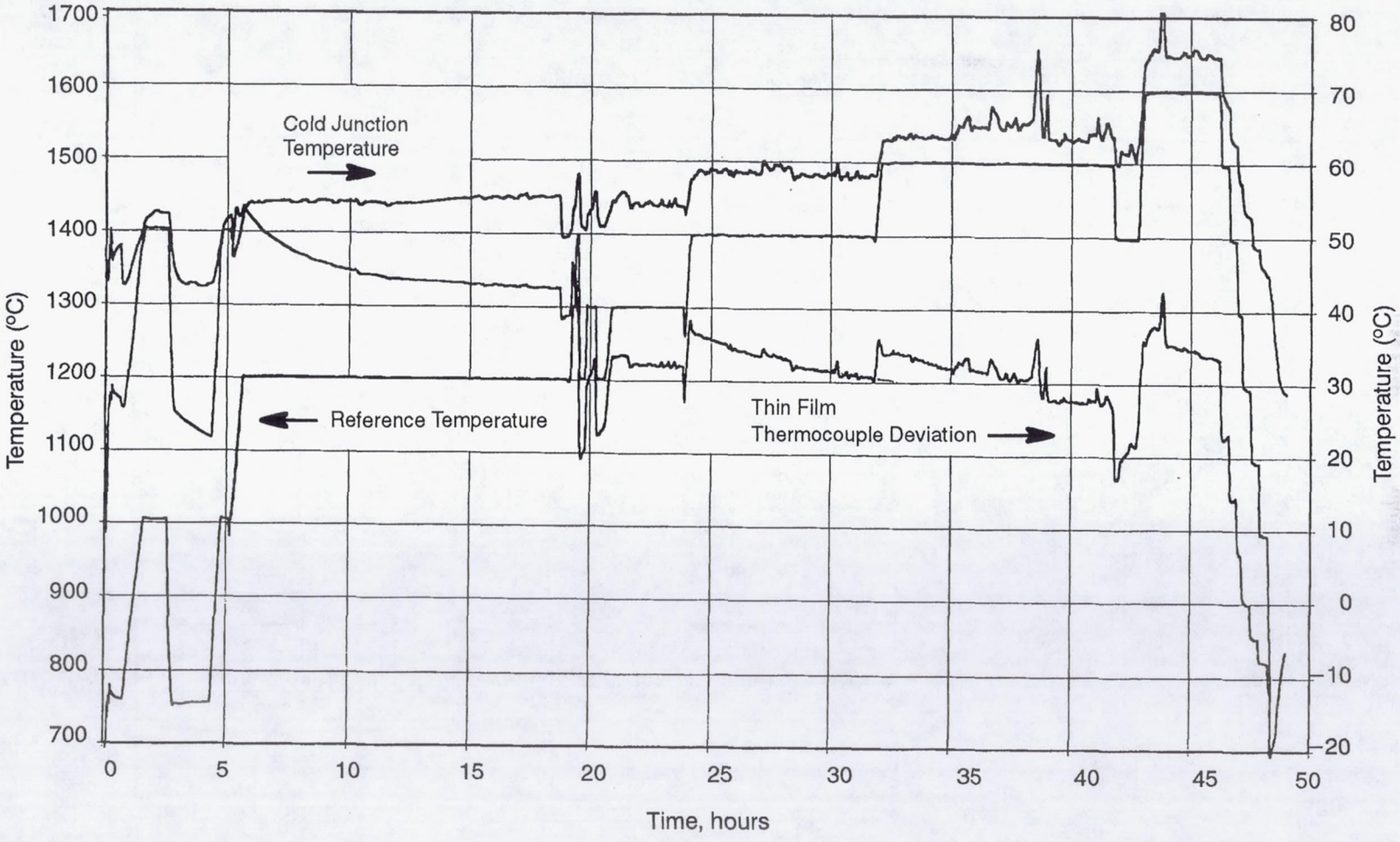

Figure 36. Thin Film Thermocouple Test.

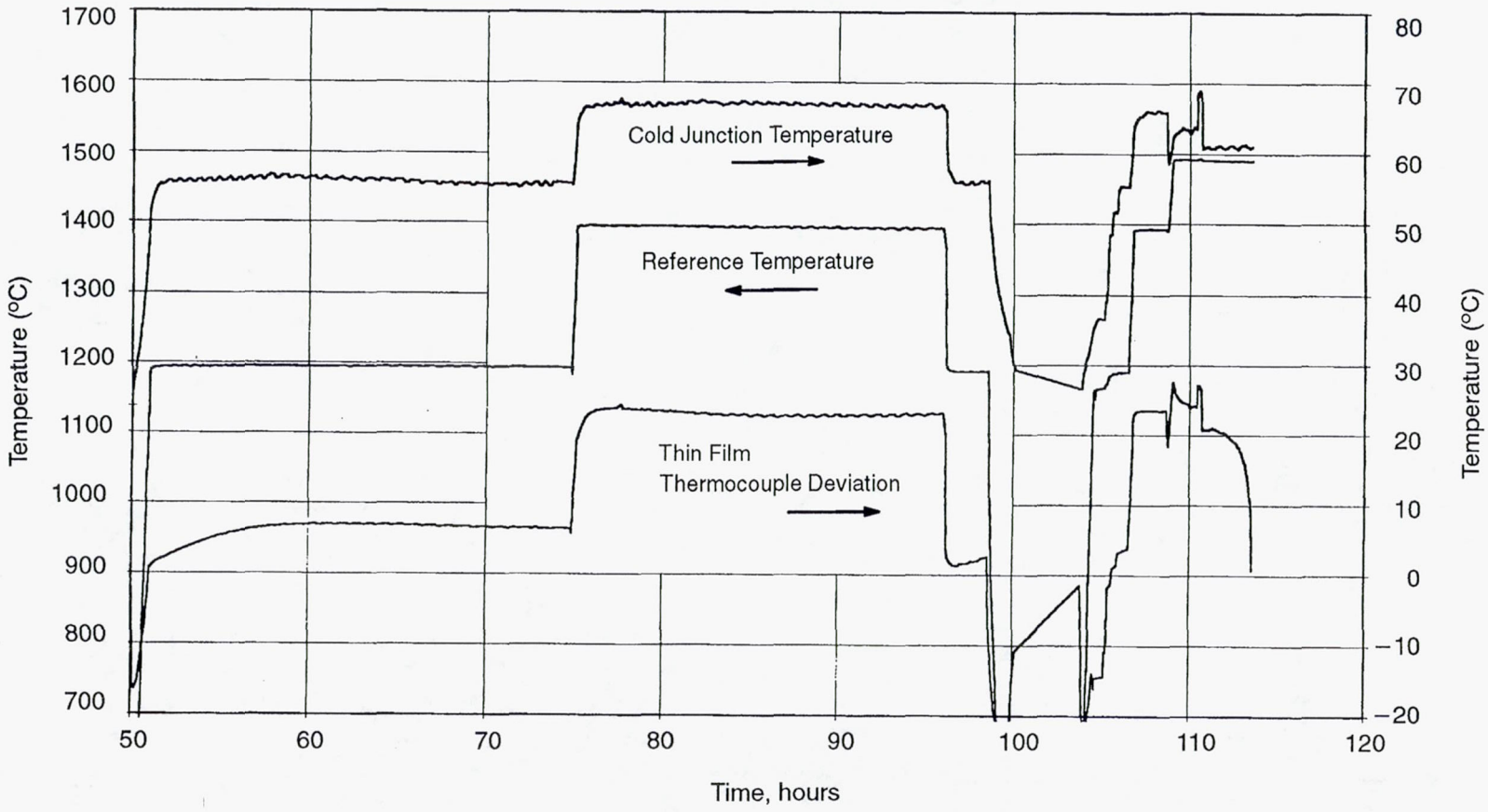

Figure 37. Thin Film Thermocouple Test.

It is difficult to draw any general conclusions based on a single thermocouple test. Consistency from sensor to sensor must be demonstrated to eliminate the necessity to calibrate each individual thermocouple. Based on this test, it can only be concluded that the thin film materials exhibited similar thermoelectric properties to the bulk material for the thin film thermocouple tested.

2.4.2.3 Thermocouple Drift

The thermocouple drift is a variation in the thin film thermocouple deviation during the holds at constant temperature (***Figures 36*** and ***37***). The cooling flow effect on the reference thermocouple caused fluctuations in the thin film thermocouple deviation making the drift data less clear but still usable. The deviation versus time plots show the nonlinear nature of the thermocouple drift. The drift data is summarized in ***Table 5***. The table contains the start time of the temperature hold, the nominal hold temperature, the time duration at temperature, the total drift for the temperature hold, and the drift rate at the completion of the hold time.

Based on the observed drift, this sensor would appear to be very usable through 1500°C. Even at 1600°C, the sensor drift was only 0.25% in 4 hours. This would be acceptable for many applications.

2.5 Conclusions

The following conclusions can be made based on the platinum alloy thermocouple work:

1. Adherent coatings of sputtered Pt6%Rh and Pt30%Rh nominally 5μm thick were achieved on both alumina and mullite substrates only after annealing at 1000°C. Subsequent heating of annealed coatings to temperatures up to 1650°C showed minor bubbling and porosity. Heating of nonannealed coatings showed major distress from bubbling, which made the coatings totally unusable.

   A change from amorphous to granular structure was observed in both alloy films at 1000°C. Stresses in the coating associated with the structure change are the probable cause for the adherence problems (large bubbles) observed in the unannealed films. We believe that annealing by slowly heating the applied films in small temperature increments allows the film structure to relieve itself before exceeding the bond strength of the film to the substrate.

2. Absolute calibration and drift testing were conducted on one Pt6%Rh to Pt30%Rh thin film thermocouple sputtered on a 99.9% alumina substrate with the cold junction < 80°C and the hot junction at the test temperature (1200° to 1600°C). The thermocouple was at temperature for approximately 100 hours. The results are summarized:

   - Deviation between the reference thermocouple (1 mm diameter platinum sheathed Type B, MgO insulated) and the thin film thermocouple was less than 40°C for all test points (1600°C maximum). The small deviation demonstrates that the thermoelectric properties of the sputtered thermocouple closely matched those of the wire thermocouple. It infers that the sputtered alloy of both legs of the thermocouple is very similar to the wire alloy legs.
   - The deviation described in the previous paragraph does not increase as a function of time at temperature (it actually decreases) even though the sputtered films are oxidizing and getting thinner. This indicates that the composition of the sputtered films are uniform through the cross section.
   - Drift (change in calibration as a function of time at a constant temperature) was evaluated at temperatures from 1200° to 1600°C. The data is summarized in ***Table 5***. Typical

Table 5. Summary of Thin Film Thermocouple Drift Data.

Start Time (hours)	Temperature (°C)	Duration (hours)	Total Drift (°C)	Drift Rate (°C/hour)
6	1200	13	+11	+0.16
24	1400	8	+6	+0.40
32	1500	10	+7	+0.20
43	1600	3	+4	+1.00
51	1200	24	–6	+0.04
75	1400	21	+1	–0.03

response was relatively high drift initially after reaching the test temperature, followed by a decreasing rate slowing to a constant rate (as reported in ***Table 5***) usually within 5 hours. The absolute drift rates are very low at 1500°C and below, and are acceptable for many measurement applications at 1600°C.

- Drift rates during the initial 50 hours of testing were significantly higher than those during the later phases of testing (50 to 100 hours). This indicates that the measurement accuracy could be improved by heating the thermocouples to temperatures above the use temperature to stabilize the thermoelectric characteristics prior to using the data.

3. In summary, the performance of the thin film thermocouple was impressive on the basis of (1) absolute agreement with the wire thermocouple; (2) low drift rate (up to the point of failure due to oxidation/evaporation at 1600°C), and (3) ability to function in a high temperature (1650°C) environment. We believe the life expectancy at elevated temperature could be extended significantly by using oxidation retarding top coats.

3.0 Silicon Carbide Thin Film Thermocouple

3.1 Background

The idea of using two different types of doped silicon carbide (SiC) films as a thermoelectric sensor was based on historical attempts to use bulk SiC as a thermocouple.[7,8] A thermoelectric potential of 200 mV/°C between two forms of SiC was reported.[8] Also, there is chemical compatibility and a close thermal expansion match between silicon carbide and many silicon-based structural ceramics with potential use in gas turbine engine hot section components. Another factor was the concern that platinum rhodium alloy thin film thermocouples (an alternate high temperature thermocouple alloy) may not function on silicon-based ceramics because of the formation of a relatively low melting point platinum silicide.

Literature references[9,10] indicated that doped silicon carbide films were most reliably produced by Chemical Vapor Deposition (CVD) processes. We did not have in-house capability to manufacture CVD SiC at GEAE but wanted to validate the concept empirically prior to committing development effort to its implementation.

3.2 Concept Validation

The technique we chose to validate this concept was based on using equipment and techniques available to us at GEAE (which did not include the preferred choice of CVD and the ability to apply dopants during the CVD process). It consisted of measuring the thermoelectric potential between two forms of SiC and a platinum rhodium alloy (Pt6%Rh). This was done (at the GEAE facility in Cincinnati, Ohio) by sputtering a 5000 Angstrom film of Pt6%Rh alloy on two bars (rectangular cross section) of different types of SiC.

- Norton, sintered SiC (NC–203), 0.64 x 1.27 x 15.24 cm.
- Raytheon, CVD SiC, 0.32 x 0.64 x 15.24 cm.

The sintering compounds in the Norton material produced the equivalent of a positively doped form of SiC. The Raytheon material was CVD SiC.

Electrical isolation between the sputtered Pt6%Rh films and the SiC bars was obtained by thermally oxidizing the SiC and then sputtering a silicon nitride (Si_3N_4) layer over the silicon dioxide (SiO_2). The basic steps in manufacturing the SiC/Pt6%Rh thermocouples were as follows:

- Heat the SiC bars in air at 1000°C to form 1000–3000 Angstrom thick silicon dioxide layer.
- Remove silicon dioxide at one end for 0.32 cm length by chemically etching with hydroflouric acid.
- Sputter a 5 μm thick silicon nitride film over the silicon dioxide with a mask over the area where the silicon dioxide was removed.
- Sputter a 5000 Angstrom Pt6%Rh film over the silicon nitride and uncoated SiC.

This formed a SiC versus Pt6%Rh thermocouple junction at one end (hot junction) with a lead path insulated by the silicon nitride and silicon dioxide layers. ***Figure 38*** shows details of the film cross sections at the hot junction end (Zone 1) and the lead path (Zone 2) for the Raytheon coupon. Copper leads were attached at the cold end with conductive epoxy.

Both test specimens (Norton and Raytheon) were tested with the hot junction inserted approximately 5.7 cm into an electric tube furnace and the cold junction immersed in water to a depth of 6.4 cm. Water temperature varied from 25° to 100°C during the test. The hot junction temperature was measured with a platinum sheathed Type B thermocouple strapped to the SiC bar with platinel wire. The original plan to test these specimens in a combustion gas environment was changed due to test facility problems.

The test data consisted of the thermoelectric output of Pt6%Rh versus Norton (sintered) SiC and Pt6%Rh versus Raytheon (CVD) SiC thermocouples. The test results for one thermal cycle to 857°C are shown in ***Figure 39***.

The thermoelectric potential for the Norton SiC versus Pt6%Rh thermocouple was 390 mV at 857°C with good linearity. A failure in the Pt6%Rh film just above the water line prevented testing to higher temperatures.

The magnitude of the thermoelectric potential for the Raytheon SiC versus Pt6%Rh was slightly higher and of the opposite polarity but was less linear. This coupon was subsequently cycled three times to 954°C and one time to 1093°C before a failure of the platinum film occurred. ***Figure 40*** shows the coupon following the thermal cycles including a close up of the hot junction.

The similar thermoelectric potential magnitude but opposite sign between the two forms of SiC and Pt6% Rh was not predicted nor was it of consequence. It was based on the choice of the Pt6% Rh alloy (which we had

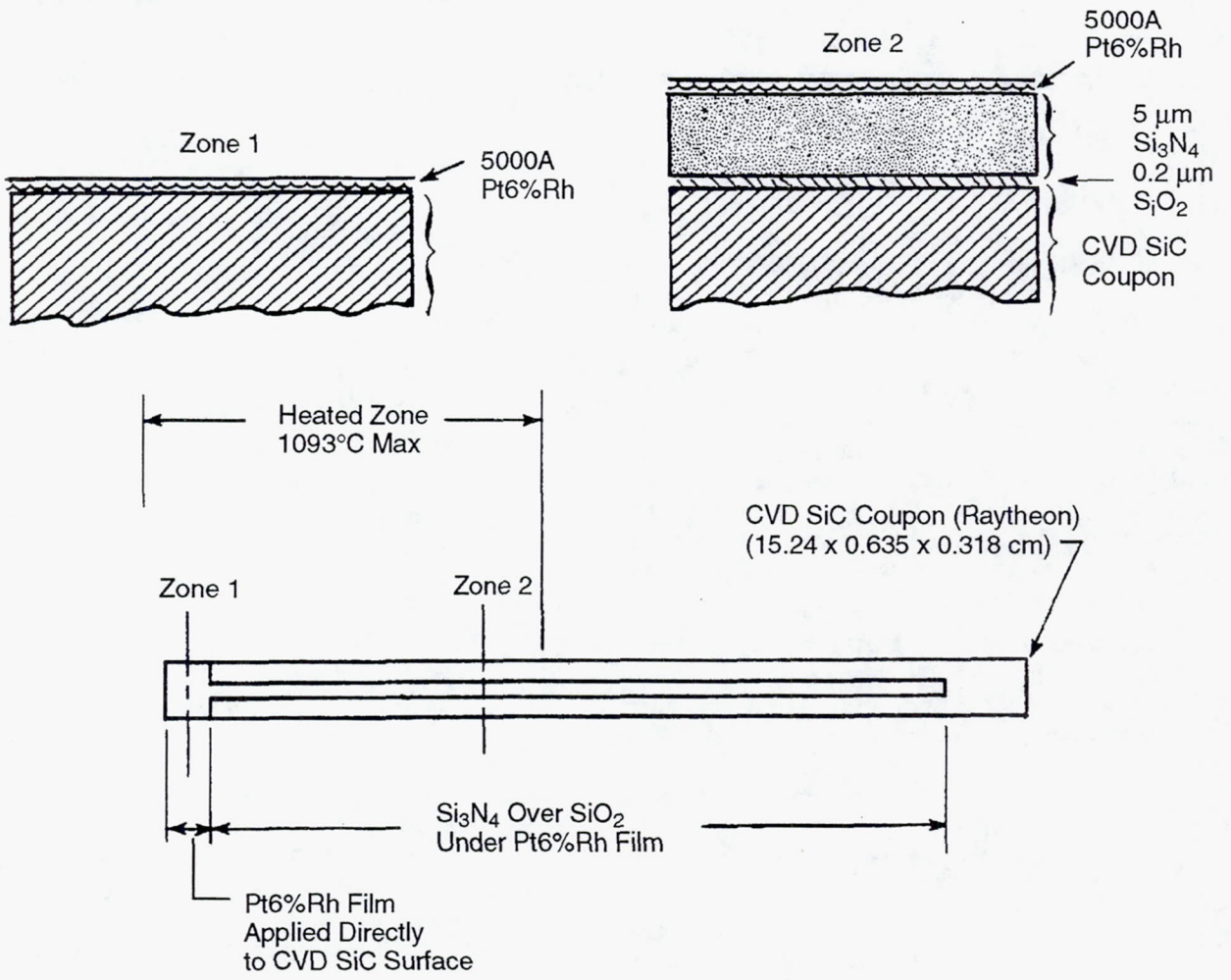

Figure 38. Concept Validation – Thin Film Application and Test Configuration.

the ability to sputter) as a reference material for measuring the total thermoelectric potential between the two forms of SiC.

The calculated thermoelectric potential between the two types of SiC was approximately 800 mV at 871°C. This represents a Seebeck coefficient of approximately 25 times that of a conventional type K (chromel/alumel) thermocouple and encouraged the continued development of this concept.

3.3 Thin Film Sensor Fabrication

A plan was developed to manufacture working thermocouples from "P" and "N" doped SiC films on CVD SiC (electrically conducting) and silicon nitride (electrically nonconducting) substrates. CVD silicon nitride was selected as the insulating layer between the sensing films and the conducting substrate. Raytheon Inc. was chosen as a subcontractor to manufacture the CVD films and SiC substrates.

The plan included the following steps related to the manufacture and testing of coating evaluation coupons and working sensors.

- Fabricate evaluation coupons of silicon nitride insulating films on CVD SiC and graphite substrates and test the coupons for maximum operating temperature and resistivity. Graphite substrates were eliminated from the plan for reasons described hereafter.
- Fabricate evaluation coupons of "N" and "P" doped SiC films on silicon nitride, aluminum nitride, and boron nitride substrates, and test the coupons for maximum operating temperature and resistivity (target value less then 0.1 ohm–cm). Boron nitride

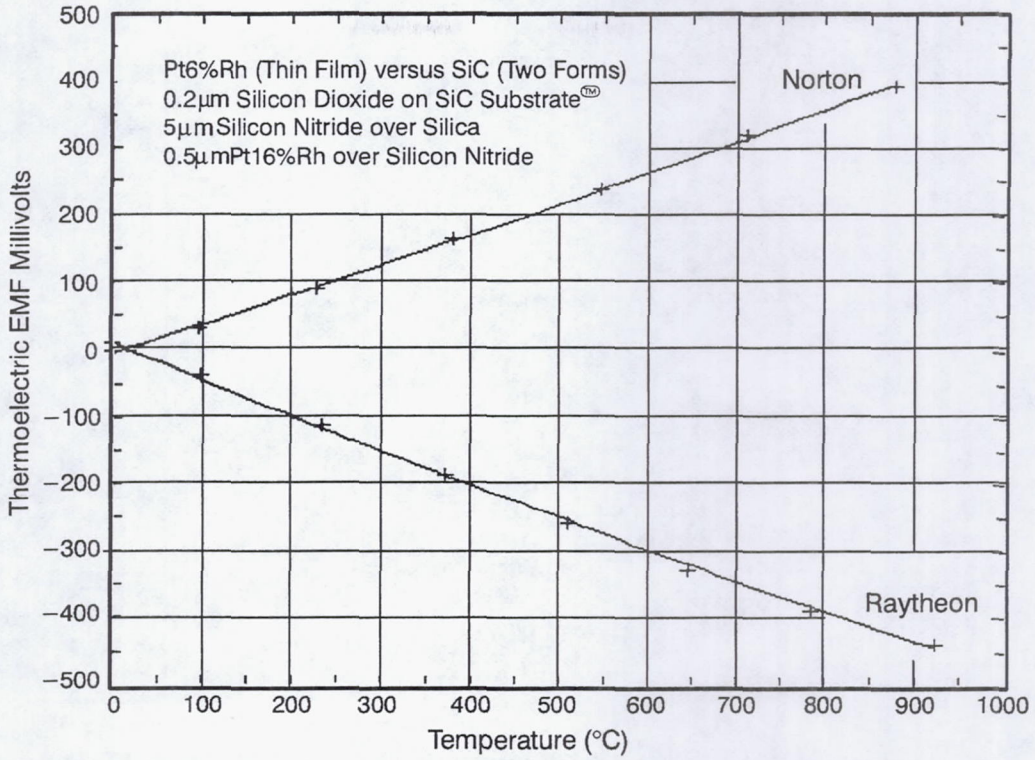

Figure 39. Thermoelectric Output versus Temperature for Two Forms of SiC versus Pt6%Rh.

was later dropped from the plan because of its limited potential as a hot section structural material.

- Fabricate thermocouple circuits consisting of "P" and "N" doped SiC on silicon nitride substrates and test the thermocouples for thermoelectric potential versus temperature, drift as a function of temperature, and maximum operating temperature.
- Fabricate thermocouple circuits consisting of "P" and "N" doped SiC on SiC substrates with an intermediate insulating layer of CVD silicon nitride and test the thermocouples for thermoelectric potential versus temperature, drift as a function of temperature, and maximum operating temperature.

3.3.1 Silicon Nitride Insulating Films

Five coating runs of CVD silicon nitride were made by Raytheon Inc. and the coupons delivered to GE for testing. The coating thickness was varied from 14 to 31 μm. The first group included some CVD silicon nitride films on both SiC and graphite substrates. The graphite substrates were selected to match the thermal expansion coefficient of the silicon nitride. They were intended to be used only for diagnostic purposes in the event that adherence problems were encountered with the SiC substrates. The adherence of the silicon nitride films to the graphite was very poor. Since there was no intention of using graphite substrates for working sensors, no further work was done with this substrate.

Film resistivity as a function of temperature was measured up to 870°C for a CVD silicon nitride film on the SiC substrate. The technique involved applying a Pt6%Rh film in the form of a multielement grid on top of the silicon nitride film and measuring the resistance between several of the grid elements and the CVD SiC substrate. The results are shown in ***Figure 41***. The measured resistivity values agreed with published values[11,12,13] within the tolerance of the measurement technique.

Although film adherence was excellent for all CVD silicon nitride films on SiC substrates, there were cracks in the as deposited films that became larger following exposure to elevated temperature. ***Figure 42*** shows a typical crack pattern as deposited. ***Figure 43*** shows a typical crack pattern after thermal exposure to 1593°C.

The cracks occurred on all samples. (The cause for the cracks is discussed later in Section 3.4.) As deposited, the cracks were very small and difficult to identify except at high magnification. After exposure to elevated temperature, the cracks became better defined and were clearly visible even at low magnification. The

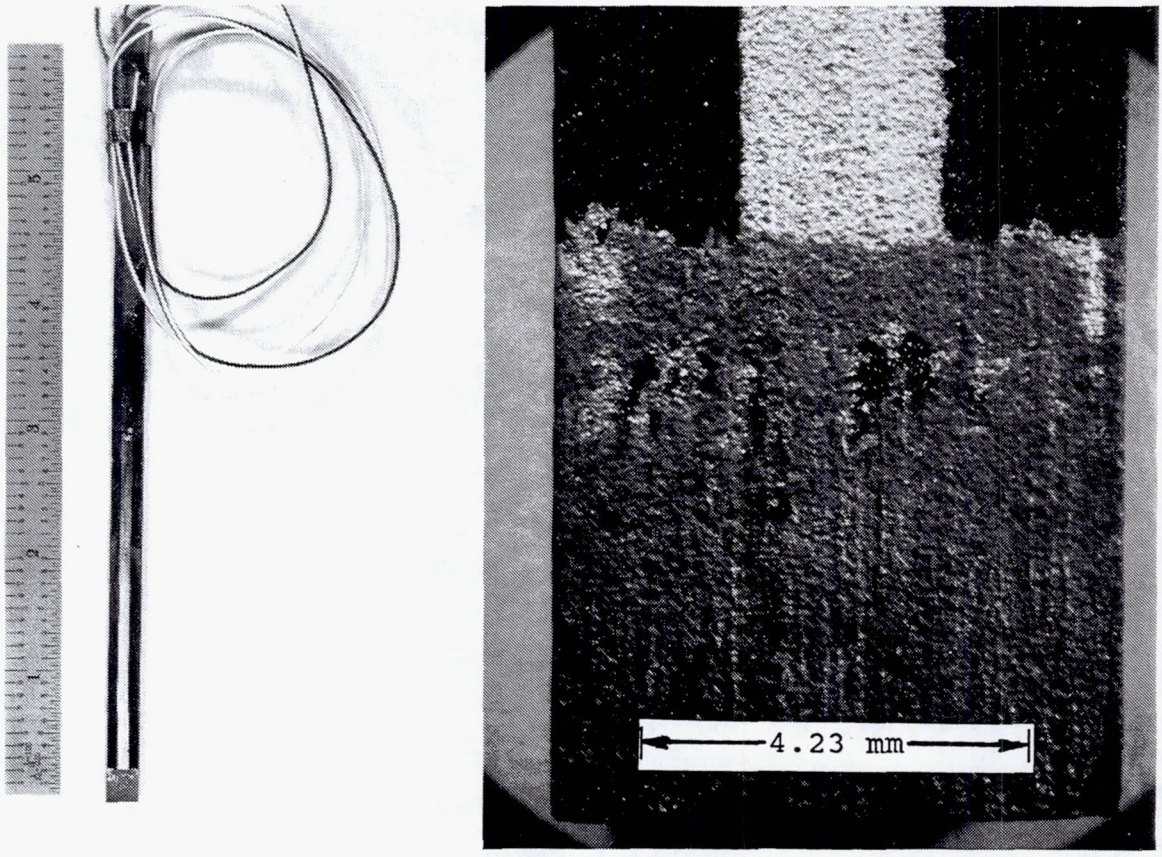

Overall View

Pt6%Rh Film Sputtered Directly over SiC Except Upper Area where Pt6%Rh Film is Sputtered over Si_3N_4 and Thermally Grown SiO_2

Figure 40. Concept Validation Coupon (Raytheon CVD SiC Substrate) Following Three Thermal Cycles to 954°C and One Cycle to 1093°C.

cracks in the silicon nitride films would almost certainly cause any doped CVD SiC sensor films applied to its surface to become discontinuous. The cracking of the coating must be eliminated before it can be used as an insulating layer for the SiC substrates.

3.3.2 Doped SiC Sensor Films

The purpose of the "N" and "P" doping of the SiC films was to provide the desired thermoelectric characteristics and to achieve resistivity values that are low compared to the shunting resistance between the sensing film and the substrate (provided by the insulating film). Literature references[9,10] indicated that stable, doped films could best be achieved by introducing the dopants as the films were being deposited. The desired resistivity for both the "N" and "P" doped films was less than 0.10 ohm–cm.

Raytheon chose to use ammonia (NH_4) for the "N" dopant and boron trichloride (BCl_3) for the "P" dopant. The preferred "P" dopant, diborane (B_2H_6), was not used because of its toxicity and the problems associated with making the gas delivery system comply with environmental regulations.

Prior to making any CVD runs with either ammonia or boron trichloride, it was necessary for Raytheon to make significant improvements in their gas delivery apparatus in order to comply with local environmental codes. These included new vented gas storage chambers, interconnecting piping, and mass flow controllers. Considerable difficulties were experienced in getting the CVD systems to work properly. Common problems included plugging in the gas delivery system, and a need to recalibrate the mass flow controllers several times.

Both "N" and "P" doped SiC films were applied to silicon nitride and AlN substrates to evaluate adhesion

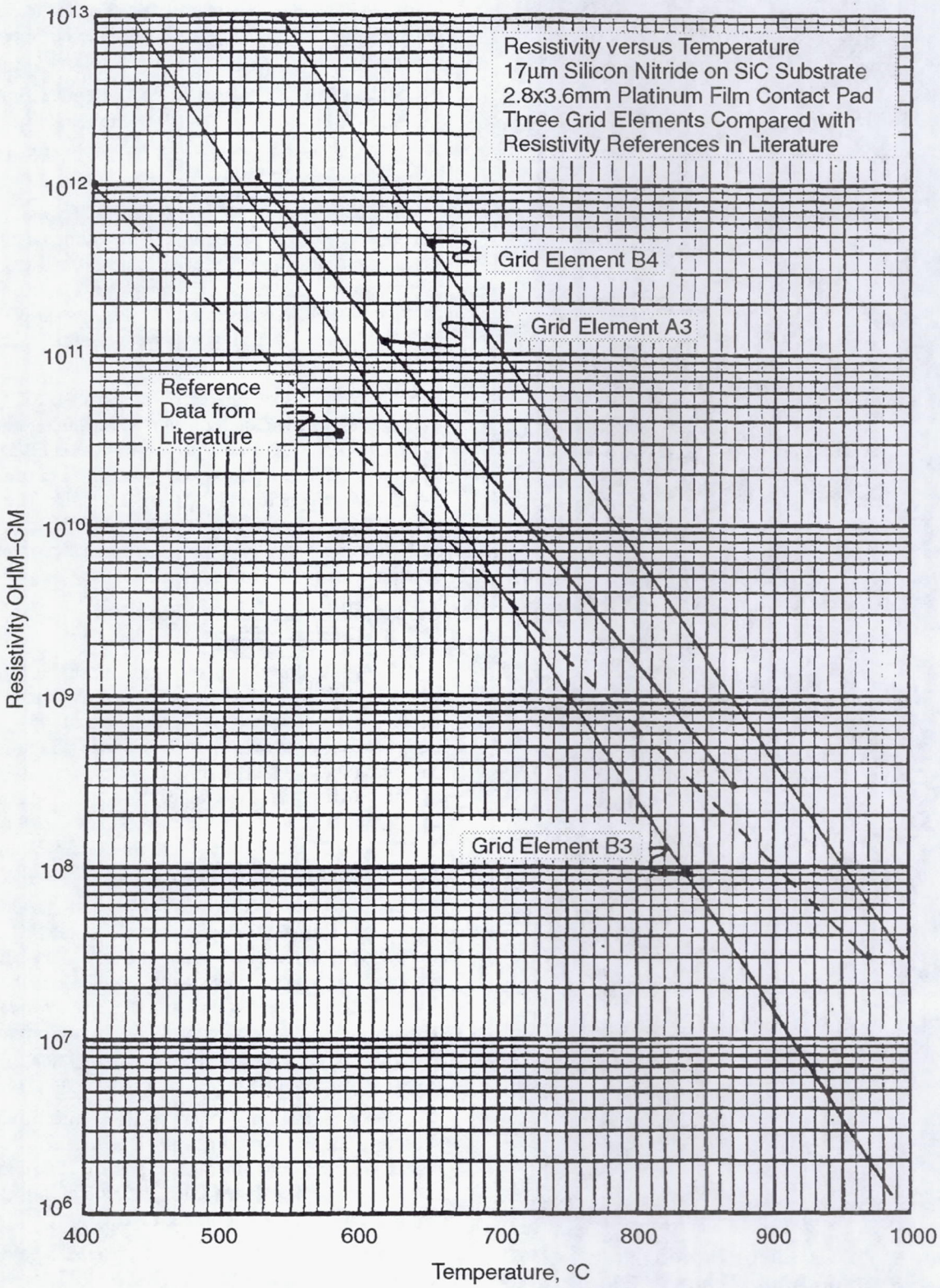

Figure 41. Resistivity versus Temperature for CVD Silicon Nitride (17 μm thick) on a CVD SiC Substrate.

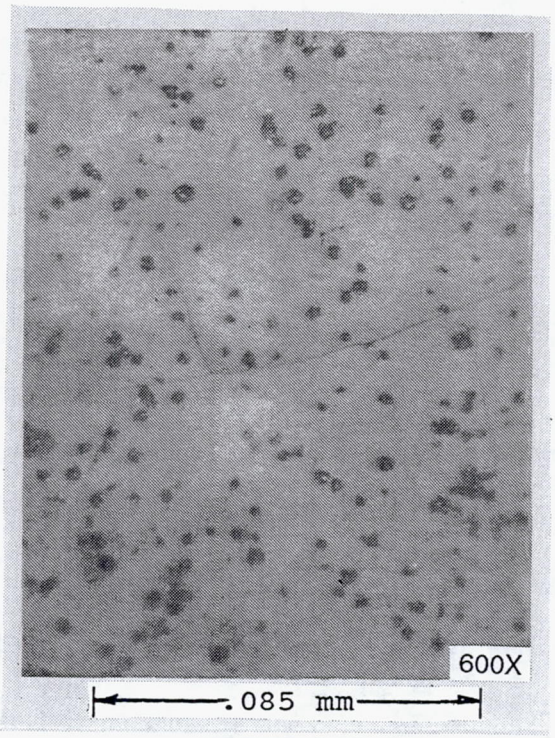

Figure 42. CVD Silicon Nitride Film on a CVD SiC Substrate – As Deposited. *(600X)*

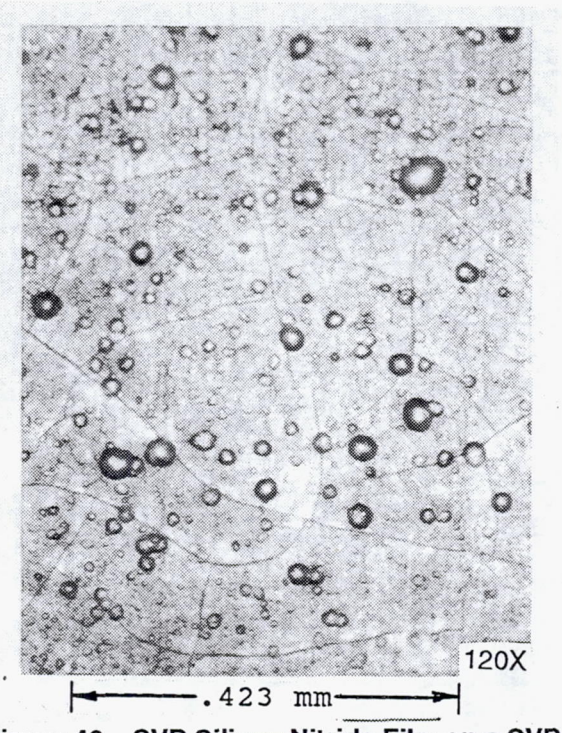

Figure 43. CVD Silicon Nitride Film on a CVD SiC Substrate After Thermal Exposure to 1195°C for 4 hours; 1482°C for 8 hours; and 1593°C for 8 hours. *(120X)*

following elevated temperature exposure, and to permit measurement of electrical resistivity. The substrate manufacturer and specifications are as follows:

- Silicon Nitride: Norton NC132, hot pressed, grain size < 2 μm, 1.27 x 15 cm, 0.64 cm thick.
- AlN: Ceratronics, tape cast, 1.02 mm thick, thermal conductivity 170 W/m–K.

Two coupon runs of "N" doped CVD SiC films were made by Raytheon on both silicon nitride and AlN substrates (four coupons of each substrate). The doped SiC coating thickness (as measured from 400X photographs of film/substrate cross sections varied from 31.3 to 62.5 μm. All substrates were nominally 2.5 by 1.3 cm.

The following coupon runs of "P" doped CVD SiC films were made by Raytheon Inc.: one run on silicon nitride, two runs on AlN, and two runs on Raytheon CVD SiC substrates. The thickness varied from 52 to 117 μm. All substrates were nominally 2.5 by 1.3 cm. The SiC substrates were added to help diagnose the cracking problem with the doped films on the silicon nitride substrates (discussed in Section 3.4).

3.3.2.1 Doped SiC Film Structural Characteristics

All "N" doped films on silicon nitride substrates showed cracks in the films prior to any thermal exposure. The cracks grew significantly after thermal exposure. ***Figure 44*** shows cracks in an "N" doped CVD SiC film on Norton NC132 silicon nitride as deposited. ***Figure 45*** shows cracks in "N" doped SiC after 8 hours at 1371°C. Film cracks were severe and consistent on all Norton NC132 silicon nitride substrates for both "N" and "P" doped films.

"N" doped SiC on AlN substrates had no visible cracks. The surface texture makes photography of the SiC films on AlN difficult and small cracks difficult to see. If any cracks exist, they are much smaller than those in the "N" doped SiC on silicon nitride substrates. ***Figures 46*** and ***47*** show as deposited "N" doped SiC coatings on an AlN substrate at two magnifications (120X and 300X). ***Figure 48*** shows this coupon after 8 hours at 1371°C.

"P" doped films on Norton NC132 silicon nitride substrates all showed cracks prior to heating. These cracks enlarged after thermal exposure. ***Figures 49*** and ***50*** show "P" doped SiC on silicon nitride as deposited and after 8 hours at 1371°C.

"P" doped films on AlN did not show cracks before or after heating. ***Figures 51*** and ***52*** show "P" doped SiC on AlN as deposited and after 8 hours at 1371°C.

"P" doped SiC films were deposited on a CVD SiC to determine if the cracking of the doped SiC on silicon

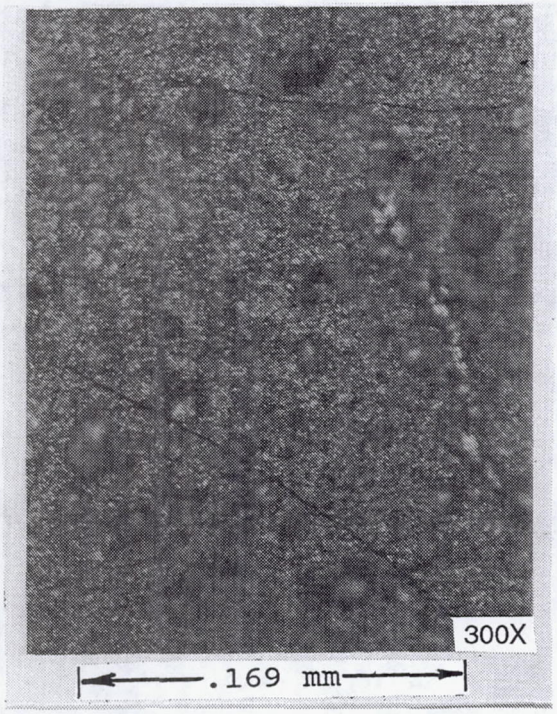

Figure 44. "N" Doped SiC on Silicon Nitride Substrate showing Cracks in As Deposited Film. *(300X)*

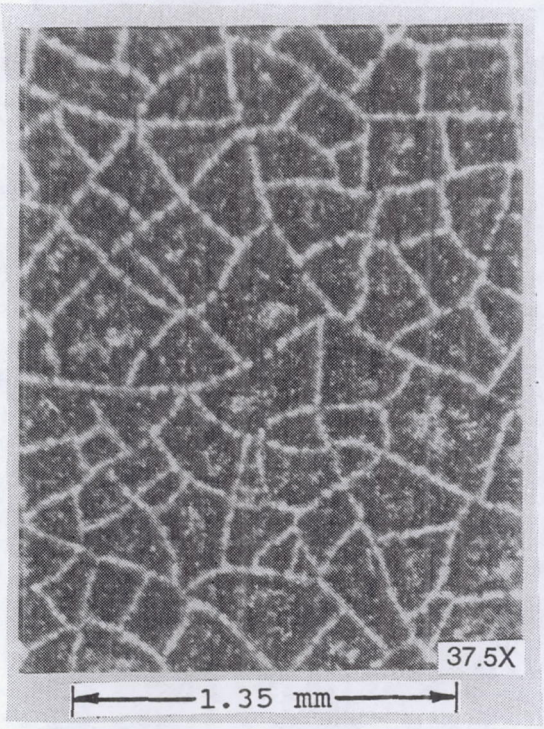

Figure 45. "N" Doped SiC on Silicon Nitride Substrate showing cracks in Film after 1371°C soak for 8 hours. *(37.5X)*

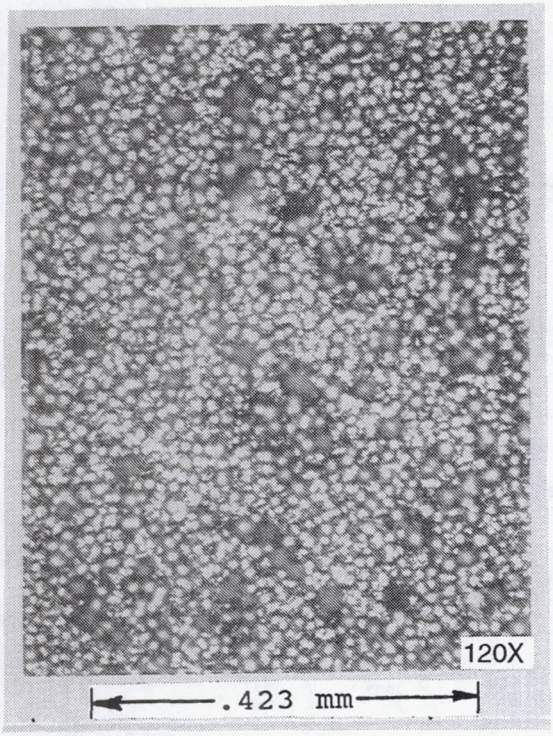

Figure 46. "N" Doped SiC on an AIN Substrate As Deposited. *(120X)*

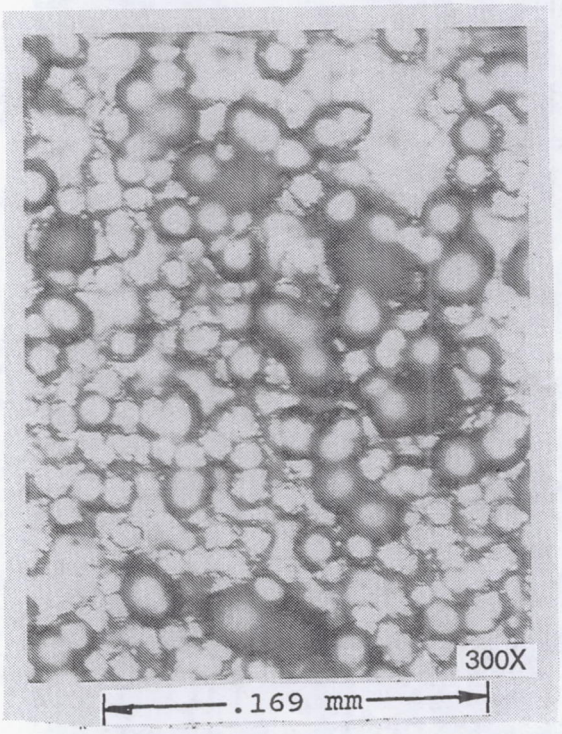

Figure 47. "N" Doped SiC on an AIN Substrate As Deposited. *(300X)*

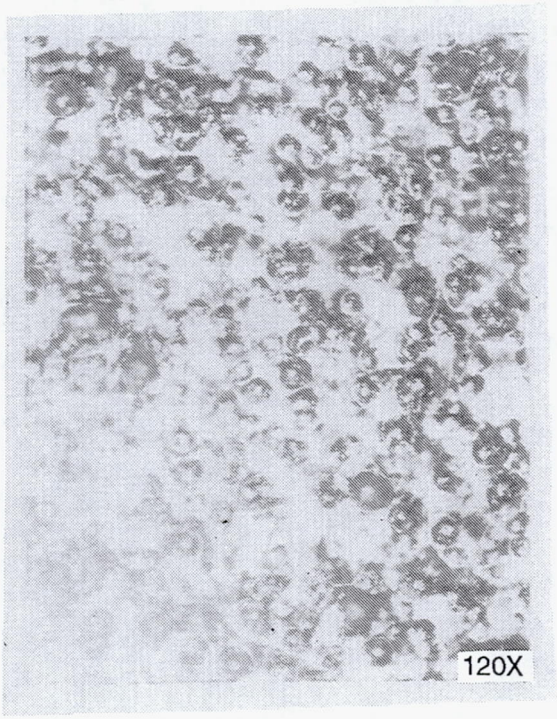

Figure 48. "N" Doped SiC on an AIN Substrate after 1371°C for 8 hours. *(120X)*

Figure 49. "P" Doped SiC Film on a Silicon Nitride Substrate As Deposited. *(120X)*

Figure 50. "P" Doped SiC Film on a Silicon Nitride Substrate after 8 hours at 1371°C. *(120X)*

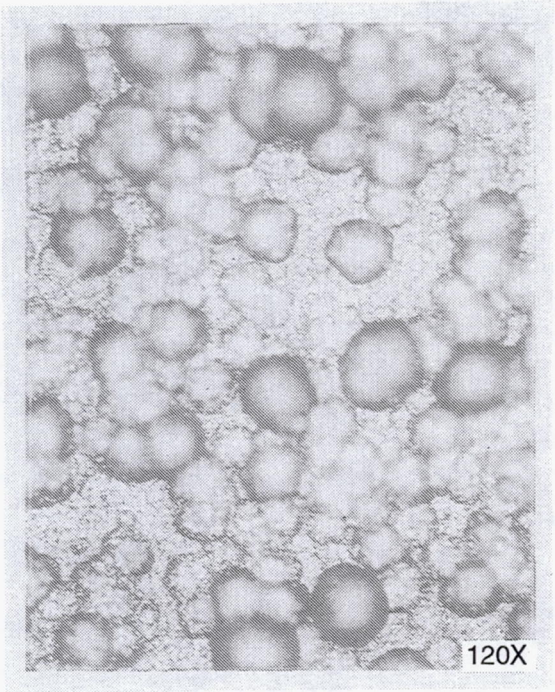

Figure 51. "P" Doped SiC on AIN Substrate As Deposited. *(120X)*

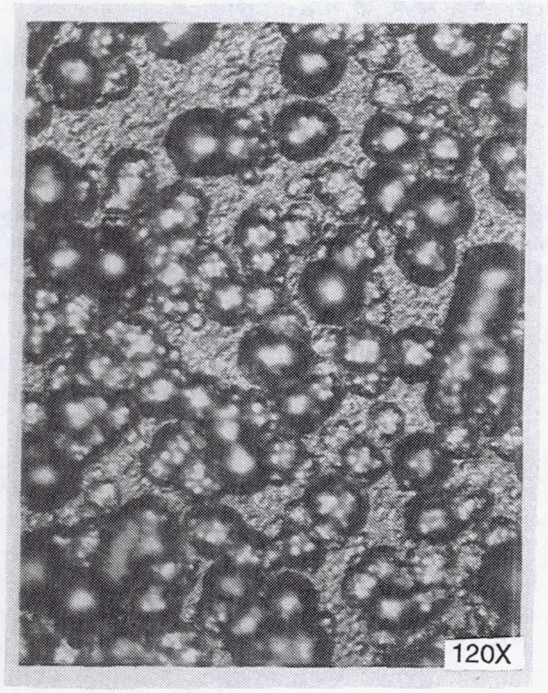

Figure 52. "P" Doped SiC on AlN Substrate after 8 hours at 1371°C. *(120X)*

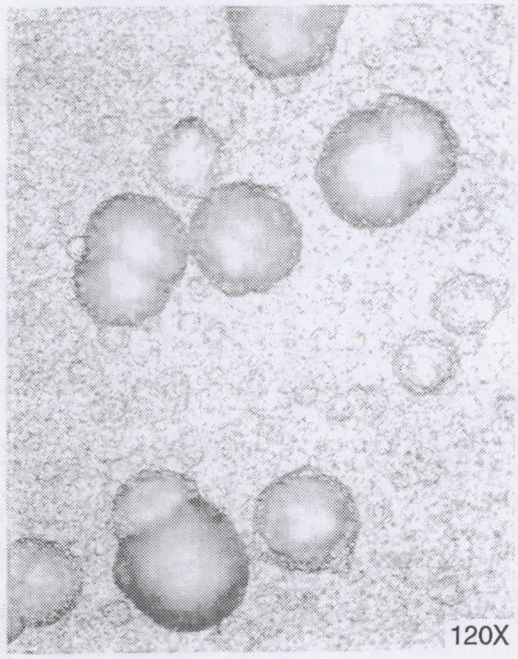

Figure 53. "P" Doped SiC on CVD Substrate As Deposited. *(120X)*

nitride was due to an intrinsic problem with the coating or an incompatibility with the silicon nitride substrate (such as thermal expansion mismatch). This would not be a viable sensor combination because SiC is a semiconductor and doped SiC thermocouples cannot be applied directly to its surface without an intermediate electrically insulating film. No cracks were visible before or after heating, indicating that there were no intrinsic problems associated with the coating process (SiC film on SiC substrate). ***Figures 54*** and ***53*** show the coating as deposited and after 8 hours at 1371°C. A detailed discussion of the cracking problem is covered in Section 3.4.

3.3.2.2 Doped Film Resistivity Characteristics

Room temperature resistivity measurements were made on samples from each batch of "N" and "P" doped SiC on both nonconductive substrates. The coatings typically extended around the edges and over part of the surface opposite the primary face. To measure the resistivity, a specific area of the primary face was first isolated by diamond-sawing through the coating around the perimeter of the primary face. A conductive epoxy or ceramic cement was then applied to either end of the coated face to provide a conductive pad for the ohmmeter probes.

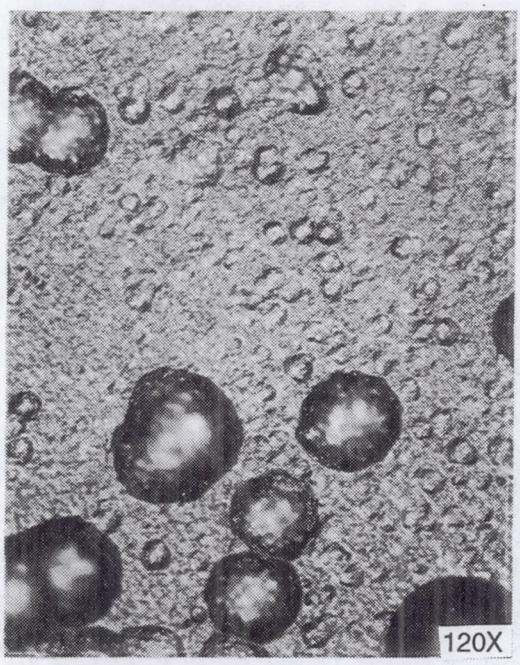

Figure 54. "P" Doped SiC on Silicon Nitride Substrate after 8 hours at 1371°C. *(120X)*

Several types of conductive cements were evaluated for this purpose including a 1000°C rated ceramic cement (Aremco 597). The high temperature cement was intended to be used for elevated temperature resistivity measurements, but was unsatisfactory. It was difficult to use and had inconsistent results. Subsequently, attempts to measure resistivity at elevated temperature were abandoned. All resistivity measurements on doped SiC films were made at room temperature using Epo–tek H20E conductive epoxy contact pads.

Table 6 summarizes all the room temperature resistivity measurements on both "N" and "P" doped films. This table also includes the film thicknesses and the configuration of the measured films used to calculate resistivity from measured resistance.

The "P" doped SiC deposited on an AlN substrate was extremely brittle and was very difficult to saw without fracturing; hence the small size for some of the configurations with this combination of coating and substrate. The reason for the brittleness has not been determined.

As indicated in ***Table 6***, the "N" doped SiC was applied with an acceptable room temperature resistivity of less than 0.1 ohm cm. The "P" doped SiC was not successful. Several attempts were complicated by CVD equipment problems resulting in very high levels of resistivity. A problem was identified with the process flow control (irregular operation of a dopant gas flow control regulator) for the "P" doped SiC. The regulator was improved and additional samples were prepared. The initial resistivity measurements of the coatings were in the range required for thermocouple fabrication on three of six samples. Microscopic examination, detailed resistivity measurements and temperature testing were not completed due to budget restraints.

3.4 Cracking of the CVD Coatings

Systems for two substrates have been investigated, silicon nitride (electrical insulator) and SiC using a CVD silicon nitride insulating layer. Cracking of the coating occurred in both CVD SiC on silicon nitride and CVD silicon nitride on SiC upon cooling from the process temperature (1300°C). A literature search and analysis to determine the cause and possible solutions to the CVD cracking problems was conducted with the following results.

3.4.1 CVD SiC on a Silicon Nitride Substrate

Analysis indicated a tensile thermal stress of 1.28E9 N/m^2 (186 ksi) could be caused by (slow) cooling from the CVD process temperature of 1300°C to room temperature due to differential thermal expansion between the substrate and the SiC coating. This did not include transient effects due to thermal gradients that could occur during a rapid cooldown cycle. Such a stress level would be high enough to cause the coating to crack.

Two possible solutions were identified. First, the deposition temperature can be reduced by changing the deposition process to plasma enhanced CVD (PECVD) or sputtering. This will reduce the stress upon post-process cooling; upon subsequent heating, the thermal stress in the coating will be compressive. In compression the coating has a much higher failure stress. The lower elastic modulus and creep mechanism at high temperature also make this a favorable solution.

Second, a graded interface was suggested by Dr. Weibold at Auburn University. The two concerns associated with this solution are the thickness of the graded interface required to reduce the thermal stress to

Table 6. Resistivity Measurements of "N" and "P" Doped CVD SiC at Room Temperature.

Coupon Number	Dopant	Substrate	SiC Thickness (μm)	Coupon Width (cm)	Distance Between Pads (cm)	Resistance (ohms)	Resistivity (ohm–cm)
NSN–1	"N"	Si_3N_4	25	1.07	2.08	9.5E+0	1.2E–2
NSN–2	"N"	Si_3N_4	25	1.12	1.88	1.3E+1	2.0E–2
NSN–11	"N"	Si_3N_4	44	1.09	1.85	3.6E+0	9.4E–3
NAN–3	"N"	AlN	25	0.94	1.90	2.6E+1	3.2E–2
NAN–11	"N"	AlN	44	1.00	1.90	2.0E+0	4.7E–3
PSN–3	"P"	Si_3N_4	52	1.12	1.96	1.1E+3	3.4E+0
PAN–4	"P"	AlN	92	1.08	1.91	1.2E+2	6.1E–1
PAN–11	"P"	AlN	75	1.27	1.91	6.3E+3	3.2E+1
PAN–23	"P"	AlN	85	0.71	0.89	2.1E+3	1.5E+1

acceptable levels and the effect of graded interface on the thermocouple calibration and drift.

3.4.2 CVD Silicon Nitride on a SiC Substrate

Analysis indicated a compressive thermal stress of 1.08E9 N/m^2 (156 ksi) upon cooling from the CVD process temperature of 1300°C to room temperature. This is a high compressive stress but should not be sufficient to cause cracks in the coating. Several articles[12,13] indicated that CVD silicon nitride exhibits high growth stresses that are very dependent on the process parameters. These growth stresses, in combination with the high thermal compressive stress, are most likely the cause of the cracking in this system.

The solution to this problem requires a technique to measure the coating stress in order to analyze the benefit of process parameter changes. Several techniques are described in the literature. In the most straightforward method, the coating is deposited onto a thin flat disk and the curvature of the disk is measured after coating to determine the coating stress.

3.5 Conclusions

The concept of a doped SiC thin film thermocouple was experimentally validated. Both "P" and "N" type doping of SiC during CVD deposition were successfully demonstrated. Cracking of the coating occurred in both CVD SiC on silicon nitride and CVD silicon nitride on SiC upon cooling from the process temperature (1300°C). Analysis was conducted to determine the cause of the cracking and possible solutions were suggested. Work was stopped because available funding for this portion of the program was expended.

4.0 Long/Short Wave Length Radiation Measurement

4.1 Introduction

Our primary focus at GEAE is the development of measurement systems for use on propulsion systems. Radiation pyrometers are commonly used to measure metal component temperature. The pyrometer systems generally use a silicon photodiode as its detector. These devices are sensitive to radiation in the wavelength range from 0.4 to 1.1 μm. The silicon detectors are desirable because they are:

- Fast (100 kHz)
- Stable
- Rugged
- Easily compensated for ambient temperature variation.

A typical application is the temperature measurement of rotating (12,000 rpm) turbine blades. In this application, the pyrometer can resolve the individual blade temperature profiles as they pass through the pyrometer's line of sight.

Pyrometers are also used extensively in material development and testing applications. A large variety of specialized applications have been developed. Each application requires consideration of the required speed, accuracy, wavelength range, and mounting constraints. The focus of this report is on propulsion system measurements – our primary area of expertise and interest – but most of the concepts are equally applicable to material development and testing applications.

The metallic superalloys used in hot section components have the following desirable radiative properties:

- In this wavelength range (0.1 to 1.1 μm) most of these materials have stable high emissivities (0.8 to 0.9) and, therefore, low reflectivity (sum of emissivity and reflectivity equals 1 if no transmission is present). This high emissivity provides more energy allowing a higher output, and the low reflectivity reduces errors from outside sources of radiation.
- These materials are opaque; the energy emitted comes from the surface, and is not affected by internal temperature gradients.
- These materials are typically very Lambertian, meaning they emit energy in a cosine distribution about the surface normal and they distribute energy incident on the surface in the same fashion. Thus, the measuring device is relatively insensitive to its angle relative to the measured surface.

In addition, the combustion gases through which the measurements are usually made do not emit or absorb significant energy in this wavelength range.

In this situation, radiation measurement is a good technique to determine metallic hot section component temperatures.

Some ceramic materials, such as silicon carbide and silicon nitride, have properties similar to these metals. For these materials, the standard pyrometer applications work very well. We have successfully used a silicon pyrometer on SiC coated carbon-carbon low pressure turbine blades during the course of the ATEGG program.

Other ceramic materials, such as alumina, mullite, and zirconia, do not have these favorable radiative properties in the silicon detector wavelength range (0.4 to 1.1 μm).

- They have low emissivities (0.2 to 0.5) that tend to vary with material condition – less energy is available to be measured and a high reflectivity – meaning they are very sensitive to reflected radiation from outside sources (adjacent hot parts or combustors).
- They are translucent; the energy emitted is a volume effect from within the material. The energy emitted from the surface is susceptible to the variation due to the internal temperature distribution.
- Fortunately, these materials are generally Lambertian.

The uncertainties caused by these properties make it virtually impossible to use standard silicon pyrometry for accurate temperature measurement of ceramics in propulsion system applications where hot adjacent parts or a strongly radiating combustor have a significant view factor to the surface to be measured. In addition, temperature gradients near the surface of the material can cause large errors.

Several techniques have been suggested for using radiation measurement at multiple wavelengths as a means to separate the radiance emitted from the target surface and the radiance reflected from adjacent sources. These methods use spectral information to separate the emitted and reflected radiation into two discrete curves. Once the curves are separated, the

temperature of the component can be determined. This, combined with an understanding of the translucence effects, could yield a viable system of temperature measurement. GE is actively developing a system of this type through an Independent Research and Development program (IR&D Project 7.14).[14]

Another possible solution is to select a wavelength region where the material properties of the ceramics are more desirable (high emissivity and opacity). The spectral emissivity and transmission data available for these materials shows this to be the case at both short (< 0.4 μm) and long (> 3 to 5 μm) wavelengths. Investigation of techniques for long/short wavelength radiance measurement to determine temperature is the area of interest for this section of the program.

4.2 Work Scope

The objective of this portion of the program is to investigate the possibility of using long/short wavelength measurement to determine the temperature of ceramic components in propulsion systems. The materials to be investigated are:

- 99.8% alumina (Coors)
- 96% alumina (Coors)
- Mullite composite (GEAE)
- Zirconia 8% yttria (Zircoa™)

The first issue to be addressed is to select wavelength regions where the materials have high emissivity and are opaque and where combustion gasses do not exhibit strong emission/absorption characteristics. There are indications in the literature[15] that at shorter wavelengths there is a substantial increase in emissivity of some of the subject materials (Alumina 0.35 – 0.60 at 0.4 μm; Zirconia 0.80 at 0.4 μm). Gas emission/absorption is not a problem at 0.4 μm.

The emissivity and opacity of these materials also increase as the wavelength approaches 2–5 μm (depending on the material) and remain high through at least 11 μm. In the range from 2 to 8 and from 9 to 11 μm, there is very strong gas emission; but there is a low emission region in the area from 8 to 9 μm.

The following are the items that will be evaluated in the silicon detector wavelength range and also the two wavelength regions selected for investigation.

- Fabricate measurement systems in the required wavelength ranges and evaluate the potential for use in propulsion systems.
- Measure the emissivity of the materials.
- Measure the radiance from the material in the presence of hotter adjacent sources.
- Compare the measured data with calculated values and evaluate the benefits of using short or long wavelength measurements.
- The emission/absorption of combustion gases is low in the 8 to 9 μm band but may still cause large errors as pressure is increased above atmospheric. The effect of emission/absorption as a function of pressure in this spectral band will be investigated.

4.3 Thermogage™ Emissometer

This section describes the equipment used to conduct the emissivity and reflectivity measurements. The purchase of all equipment and any subsequent modifications for this portion of the program were funded by GE. The details are included only to inform the reader of the state of the equipment when the data was taken.

Several methods for measuring emissivity and evaluating the effect of reflected radiation were considered. Finally, a packaged system, known as a "bang-bang" emissometer, was purchased from Thermogage Inc. It was decided that the emissometer would have a radiant energy source added by GE to illuminate the specimen for the evaluation of the effects of reflected radiation. This addition is described in Section 4.3.6.

The Thermogage™ system consists of a graphite tube that is resistively heated, electronics to support this task, and a pneumatically actuated graphite rod and specimen cup assembly that are centered in the tube furnace; but does not touch the tube walls (***Figure 55***). The graphite tube is purged with an inert gas (nitrogen) to prevent oxidation, and the support and enclosing structure are water cooled. During actuation, the specimen cup quickly travels from the center of the furnace to the end of the cool graphite end cap (30 cm).

The theory behind this technique of emissivity measurement is that while the specimen is in the center of the furnace, the walls of the tube and specimen approximate a black body cavity. This is true if the sample and an adequate length of tube wall in front of the sample have a uniform temperature. How well this system approximates a black body is discussed in Section 4.3.1. When the specimen is actuated, it leaves the heated portion of the furnace and there is no longer any reflection from the furnace walls. Only the energy emitted from the specimen reaches the measurement device. By definition, the normal emissivity is the ratio of energy emitted by a material to the black body emission at the same temperature. The normal

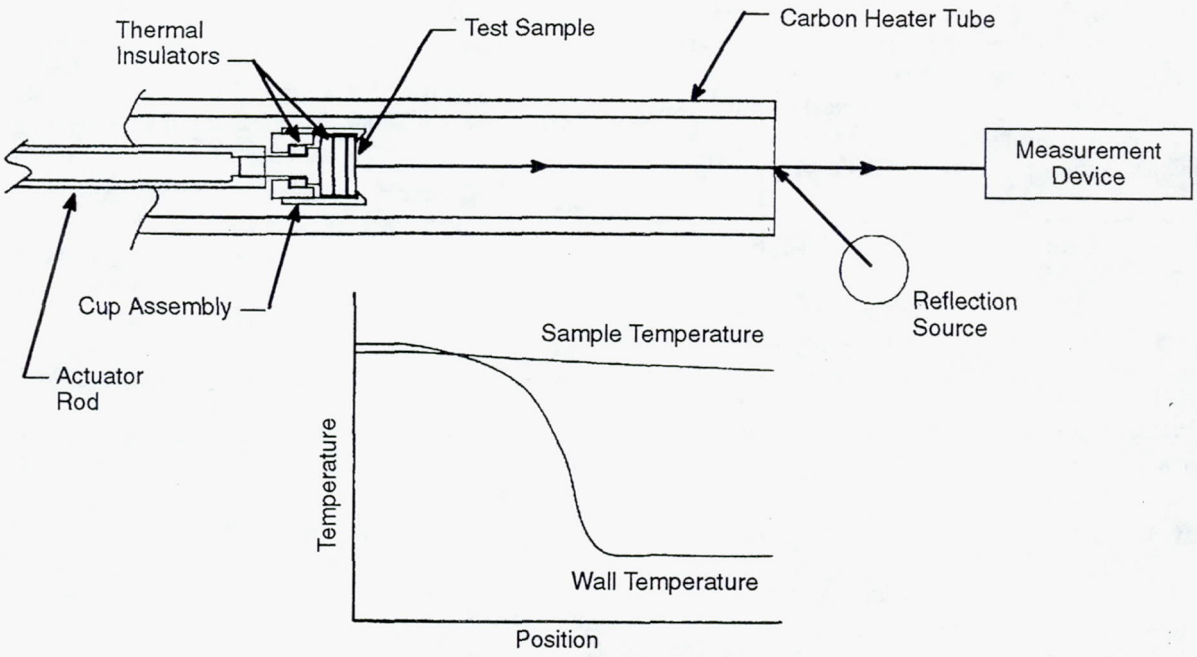

Figure 55. Thermogage℠ Emissometer Schematic.

emittance of the material can be calculated as the ratio of the radiance measured when the specimen is outside the heated section to that measured when it is located in the heated black body cavity.

Several problems were encountered with the Thermogage℠ system that required modification of the unit or corrections to the data. In addition, the radiance source was added and some enhancements were made to the system.

The following sections describe the modifications made to the Thermogage℠ system before the data was taken.

4.3.1 Black Body Cavity

Fundamental to the emissivity measurement using this technique is that the sample and tube wall form a good approximation of a black body cavity. This requires that the sample and the tube wall have a uniform temperature for an adequate length in front of the sample.

During initial checkout, a difference of 22°C was found between the sample temperature and the temperature of the tube wall used to form the black body cavity. This temperature difference would cause large measurement errors, particularly for low emissivity samples. (For wavelength = 1 μm, temperature = 1100°C, actual emissivity = 0.2, the measured emissivity would be 0.174.) The temperature difference was attributed to conduction along the actuator rod. The cup assembly was modified to incorporate an insulating spacer and the actuator rod cross section was reduced. These modifications reduced the temperature difference between the sample and the graphite tube wall to less than 3°C.

The sample temperature and the temperature gradient along the length of the tube in front of the sample were measured using a fine wire thermocouple. From the measured sample temperature and the tube gradient, the radiance of the cavity was calculated and compared to the theoretical black body radiance at the sample temperature. The calculation was performed at several wavelengths covering the range of interest. The results are shown in ***Table 7***. This was considered to be acceptable.

Table 7. Difference in Thermogage℠ Radiance from Black Body.

Wavelength (μm)	Difference in Radiance from Black Body (percent)
0.5	–1.0
1.0	–0.1
8.0	+0.3

4.3.2 Sample Specularity

The assumption implicit in the previous calculation is that the sample and tube walls are Lambertian. A Lambertian reflector distributes the energy incident on

its surface in a cosine intensity distribution. A specular reflector, on the other hand, does not distribute the incident radiation but reflects it at the incident angle. If a sample were completely specular, none of the energy incident on the sample from the tube wall would reach the cavity exit and therefore only the energy emitted by the sample would be measured.

Most materials have both Lambertian and specular components. The reflective characteristics of each sample to be tested were measured. Fortunately all the samples chosen (alumina, mullite, zirconia) had a relatively small specular component (< 7%). The emissivity data was analytically corrected for this effect. The emissivity of samples with a large specular component cannot be accurately measured by this technique.

4.3.3 Sample Cooling

Another fundamental assumption on which this technique for measuring emissivity is based is that the sample does not cool appreciably as it is actuated outside the cavity. The rate of cooling can be inferred from the slope of the measurement trace (***Figure 56***) after the sample is actuated past the hot section of the furnace. This slope indicates that significant cooling is present.

To reduce the effect of cooling on the measurement, the time it takes for the sample to exit the cavity was reduced from 200 to 120 ms. Even with this modification, there was still significant cooling observed. It was desired to correct the radiance measured at the exit of the hot zone to the level of emission when it was still in the cavity.

To accomplish this, a one-dimensional finite element heat transfer analysis was conducted. Several combinations of sample thickness, total emissivity, and thermal conductivity were evaluated. This analysis shows that a linear extrapolation of the slope after the sample has exited the hot section of the furnace back to the time when the sample is just starting to leave the cavity can be used to correct the radiance of most samples. Only those samples with a very low thermal conductivity cannot be corrected this way.

4.3.4 Reflection from the Cup Lip

Another fundamental assumption is that all the energy measured by the pyrometer when the sample has exited the cavity is emitted by the sample. This is not

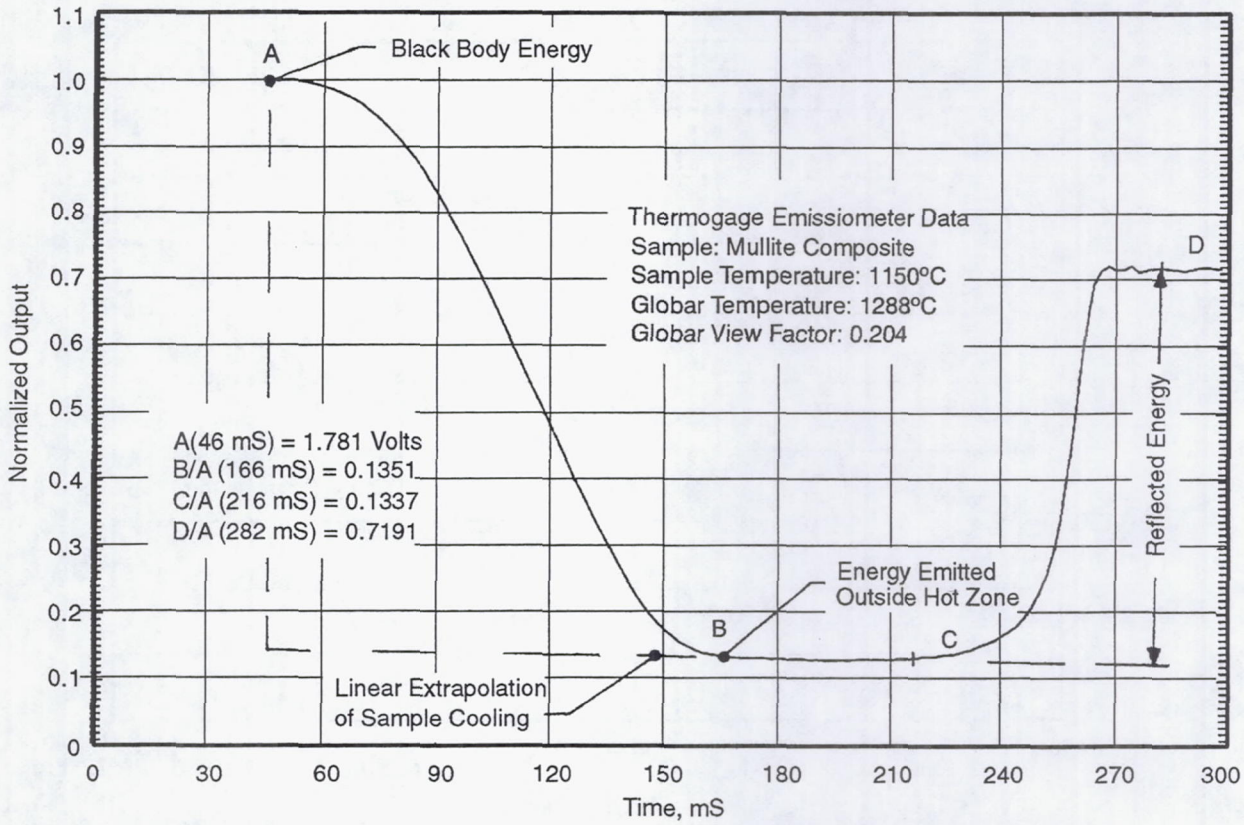

Figure 56. Normalized Silicon Detector Output versus Time.

completely true since the sample outside the cavity still has an appreciable view of the hot sample holder cup lip. The cup lip was reconfigured to provide a minimum thickness and chamfered to reduce the view factor of the lip to a minimum. Even with these changes, a correction was still required on low emissivity samples (such as cup lip height = 1.25 mm, calculated view factor = 0.03, actual emissivity = 0.20, measured emissivity 0.22, and measurement error = 10%).

4.3.5 Zirconia Oxygen Depletion

Another assumption is that the emissivity of the sample is not affected by the high temperature nitrogen environment within the black body cavity. Zirconia samples had significant changes in emissivity due to oxygen depletion. The Thermogage™ emissometer uses a nitrogen purge to protect its graphite parts from oxidation. A large change in room temperature reflectivity was observed between zirconia samples that were cooled from elevated temperature in air versus those cooled in the nitrogen environment (0.82, 0.34, respectively). This difference was attributed to oxygen depletion of the zirconia surface. The other materials for which emissivity measurements were made (alumina, mullite) did not exhibit this effect.

To correct this problem, the emissometer's graphite components were coated with an oxidation-resistant CVD SiC coating. This enabled the zirconia-based samples to be tested in air.

4.3.6 Reflection Source

In order to demonstrate reflected energy effects, a fixture was fabricated to hold a 1.9 cm diameter Globar (Carborundum Inc. trade name – SiC-resistive heating element) in front of the specimen at the full extension of actuation. The Globar has a heated length of approximately 20.3 cm and has a temperature limit of about 1583°C (2800°F).

During initial checkout, it was determined that the radiance of the Globar in the silicon waveband was not uniform. This required a measurement of the radiance profile of the Globar, which was accomplished using the silicon pyrometer (***Figure 57***). An average radiance incident on the specimen was calculated from this profile and the view factor of the Globar to the specimen.

A computer program was written to calculate the view factor of a small element of the Globar surface to the specimen. The program combined these view factors and the measured radiant profile to calculate the radiant

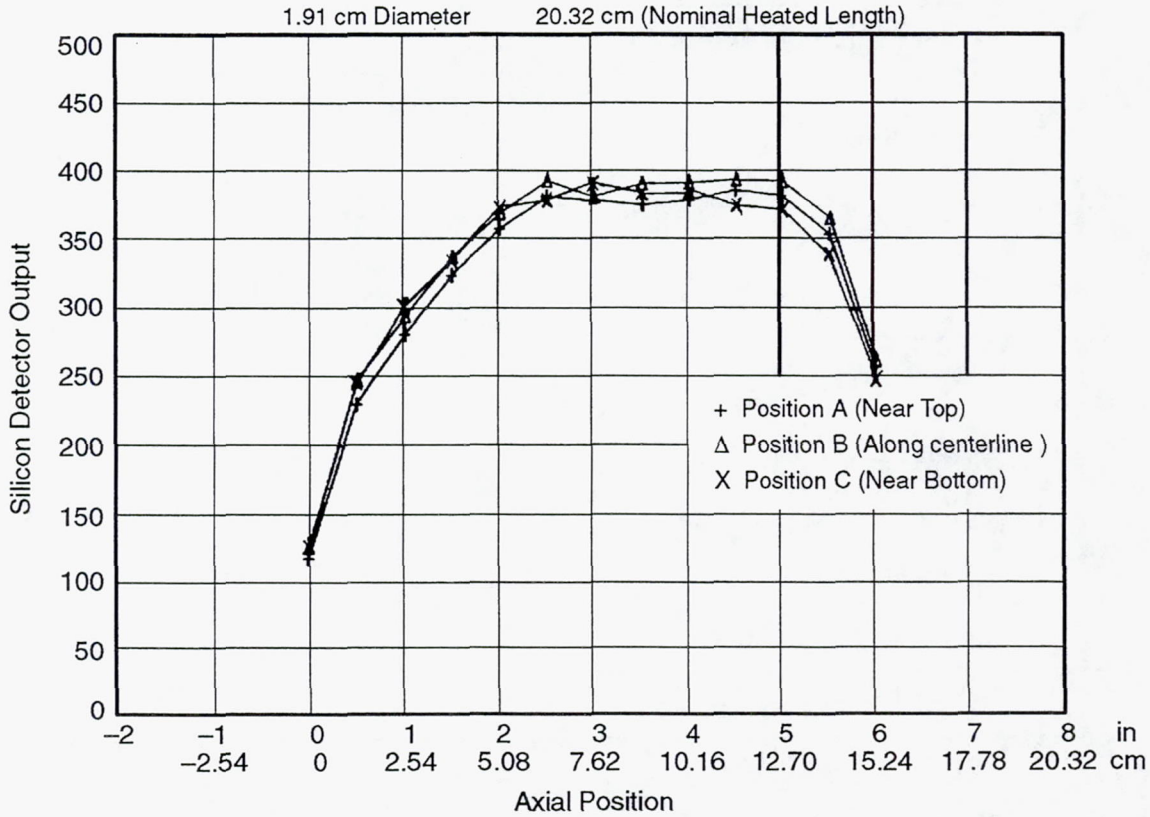

Figure 57. Globar Distribution.

contribution of each element. These contributions were summed to give a total radiant contribution at the surface of the specimen.

Variations between the characterization test and subsequent tests were handled by measuring the radiance at a specific axial and circumferential position and adjusting the Globar characterization data accordingly.

4.3.7 Data Acquisition System

A data acquisition system was assembled and acquisition software written to enable efficient measurement and display of data. The data acquisition system consists of a Jameco™ IBM "AT" compatible computer with a Metrabyte™ DAS-20 A/D expansion card running at 20 kHz. The description of a typical emittance test follows. The furnace is purged with gaseous nitrogen, heated to the desired temperature, and allowed to stabilize. The data acquisition software is run. This causes the DAS-20 card to send a trigger to the emissometer which actuates the air cylinder that propels the sample out of the cavity and begins data acquisition by the computer. Upon completion of the acquisition cycle, the data can be manipulated by the computer, saved to file, and sent to a digital plotter. The software also allows a comparison of multiple tests and can be readily customized if required.

4.4 Test Results

The emissivity data is summarized in ***Table 8***. The reflectivity measurements were used as a check of the measured emissivity. The sum of the measured emissivity and reflectivity should equal 1. Agreement was obtained within 2%. This agreement also validates the methodology (Section 4.3.6) for calculating the effect of reflected radiation. The measurement instruments and test data for each wavelength range will be discussed in detail hereafter.

4.4.1 Silicon Pyrometer Test Results

The silicon pyrometer system consists of an optical head, a silicon diode, a line driver module, and a linearizer module. The linearizer is essentially used as a power supply for the line driver module as we did not use the linearizing function of the module for these tests. The silicon diode, line driver, and linearizer are the standard types used for engine testing at GEAE. The optical head incorporates a 100 mm focal length, 25.4 mm diameter uncoated fused silica lens positioned approximately 12.1 cm from the diode. There are several apertures in the probe to reduce scattered radiation to an acceptable level. The best focus of the probe is at 64.3 cm from the lens.

A sample of a typical data run is shown in ***Figure 56***. This represents the output of the silicon pyrometer looking at a yttria-stabilized zirconia sample heated to 1149°C (2100°F) with the reflected energy source (Globar) operating at 1343°C (2450°F) and located to achieve a geometric view factor of 0.20 with respect to the sample in the fully actuated position. The detector output has been normalized at "A" which represents the point where the output starts to decrease as the result of

Table 8. Emittance Measurements.

Sample Description	Temp (°C)	Emittance Silicon Detector 0.6 to 1.1 (μm)	Emittance HgCdTe Detector 8.4 to 8.9 (μm)
96% Coors Alumina	1150	0.24	0.95
Two 2.2 mm thick samples to ensure opacity	925	0.19	0.95
99.8% Coors Alumina	1150	0.23	0.90
Three 2.2 mm thick samples to ensure opacity	925	0.17	0.89
Mullite Composite	1150	0.14	0.98
Matrix: Mullite (75% Alumina; 25% Silica)	925	0.11	0.98
Fibers: Sumitomo™ (85% Alumina; 15% Silica)			
3.4 mm thick			
Zircoa™ Zirconia with 8% Yttria	1150	0.41	0.99
6.7 mm thick samples	925	0.33	0.99

the sample being actuated out of the furnace hot zone. "B" is the point where the sample has exited from the furnace hot zone and is still inside a 100°C carbon tube. At "C" the sample is still within the carbon tube near the open end. The difference in output between "B" and "C" is due to cooling of the sample (Section 4.3.3). The cooling effect was corrected by linearly extrapolating a line through "C" and "B" backwards to the time indicated by Point "A" (46 ms). The cooling slope was determined from a run where the Globar was not energized. This value is then corrected for specularity (Section 4.3.2) and cup lip (Section 4.3.4) effects to obtain the emittance of the sample.

The radiance due to the reflected energy from the Globar at the surface of the sample was calculated as indicated in Section 4.3.6. The measured reflected energy is the difference between the total radiance measured at Point "D" and the energy emitted from the sample at this time. The emitted energy is affected by sample cooling and is found by extrapolation of the cooling slope between "B" and "C" to the time at Point "D" (282 ms). The reflectivity is the ratio of the measured reflected energy to the calculated incident energy. For this case, the reflectivity is calculated to be 0.879. The sum of the measured emissivity and reflectivity is 1.011. This is a good check of both the emissivity and reflectivity measurements and also validation of the methodology used to calculate the effect of reflected radiation on the pyrometer measurement.

Data for the other samples was taken in a similar fashion. The silicon pyrometer performed well for all measurements with no significant problems.

4.4.2 Long Wavelength Test Results

Initial long wavelength emissivity data was taken with a mercury/cadmium/telluride (HgCdTe) detector in a Perkin-Elmer Mod 96 monochrometer. A reflective telescope with a 6-inch aluminum mirror was used to transfer the sample energy to the monochrometer inlet slit. A chopper was used at the inlet slit to modulate the energy. The monochrometer used coated aluminum reflective optics and a NaCl prism as the dispersive element. The detector was an EG&G Judson HgCdTe detector with a broadband window and an amplifier system. The output from the detector's amplifier was sent to a lock-in amplifier and the analog output of the lock-in was sent to the emissometer data system. This system was used to take spectral emissivity data from 1 to 11 μm.

Figure 58 shows a comparison of data obtained using the HgCdTe system and the silicon pyrometer for the dense zirconia sample. Each trace on the plot represents data from one actuation stroke and has been adjusted along the time axis to produce overlapping energy decay curves. The silicon detector wavelength was controlled by the response characteristic of the detector. The HgCdTe wavelength was controlled by the Perkin-Elmer monochrometer at 1 and 8 μm. The Globar view factor with respect to the sample disk was 0.198.

Figure 58 illustrates the dramatic increase in emittance between 1 and 8 μm and shows remarkably good agreement between the broadband silicon detector (test point ZT0329SI) and the 1 μm narrowband HgCdTe detector test point (ZT033110). The effect of the Globar for the 8 μm test point (ZT033580) is so small that it appears identical to the other 8 μm point (ZT033380) where the Globar was not energized. This data is shown only to illustrate the points mentioned above; it was taken before the problem with oxygen depletion was understood. The data points were repeated with the revised system described below in an air environment.

Because the monochrometer and telescope optics of this system were very bulky and difficult to align, it was eventually superseded by a long wavelength pyrometer that used the same HgCdTe detector. The long wavelength pyrometer system consists of an optical head, a light chopper, an HgCdTe detector, a preamplifier, and a lock-in amplifier, as shown in ***Figure 59***. With the exception of the optical head, all of the above items were purchased from EG&G. The optical head consisted of an uncoated plano-convex ZnSe lens (27.9 mm diameter, 127 mm focal length at 10.6 μm) positioned 16.5 cm from the detector surface, and an 8.3 to 8.9 μm (8.65 μm effective) bandpass filter located 8 mm from the detector surface. There are two apertures in the optical head to reduce scattered radiation to an acceptable level. The focus of the optical head is 64 cm from the lens, with greater than 98% of the measured energy coming from within the 5.1 mm diameter spot. The chopping frequency was 3 kHz for all tests.

All of the data presented in this report was taken with this system. The zirconia samples were run in air due to the problem with oxygen depletion (Section 4.3.1.5). The methods for processing the results were similar to those described for the silicon pyrometer and will not be repeated.

4.4.3 Short Wavelength Test Results

An EG&G Optical Multichannel Analyzer (OMA) system was used for visible and ultraviolet measurements (***Figure 60***). This system consisted of a quartz lens (25.4 mm diameter, 88 mm focal length at 0.589 μm) Schott KG5 and BG39 filters and an 8 meter long

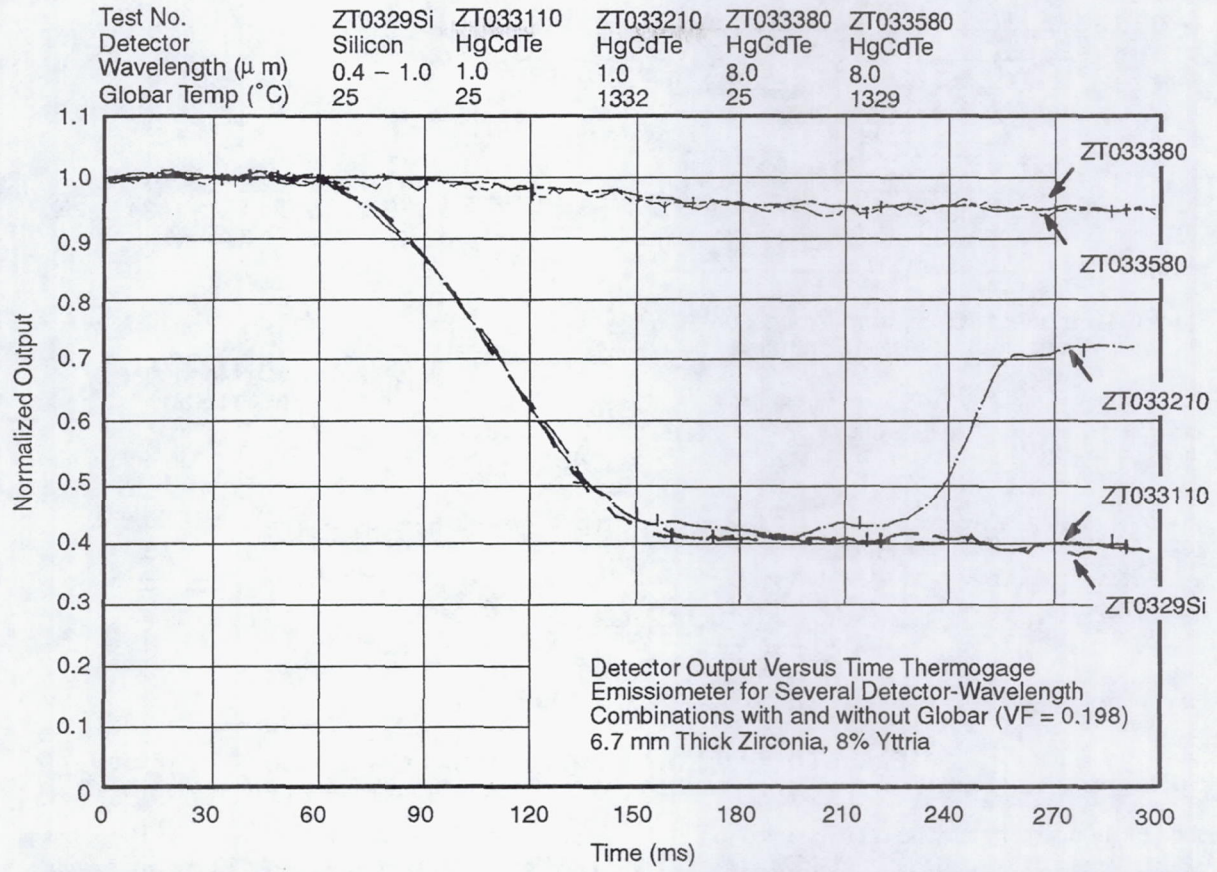

Figure 58. Detector Output versus Time Thermogage™ Emissometer for Several Detector-Wavelength Combinations with and without Globar (VF = 0.198) 6.7 mm thick Zirconia, 8% Yttria.

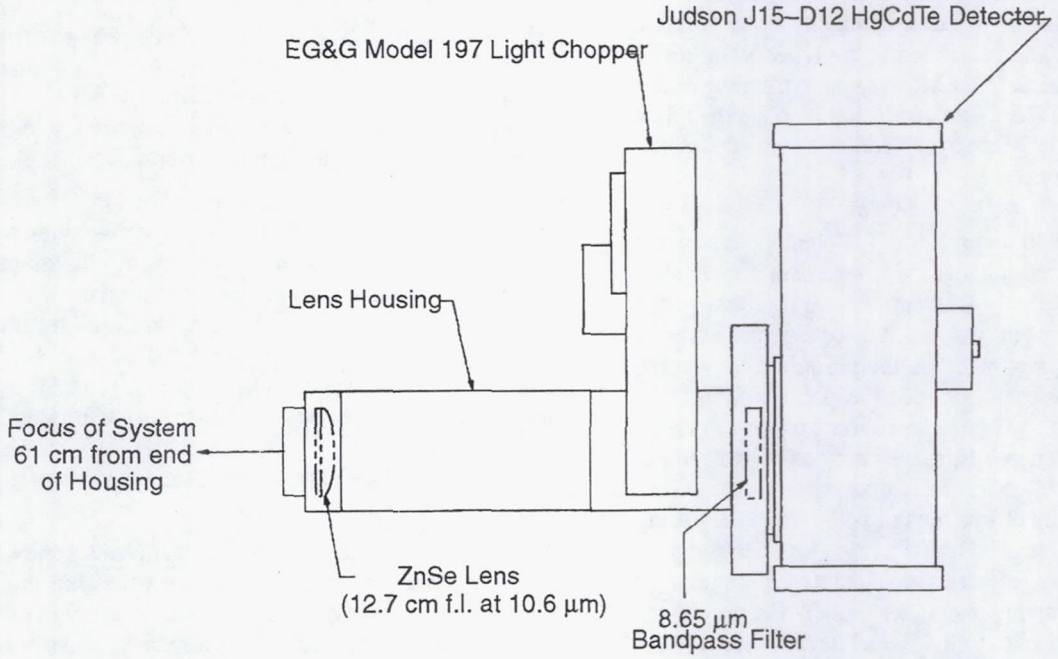

Figure 59. Long Wavelength Pyrometer Schematic.

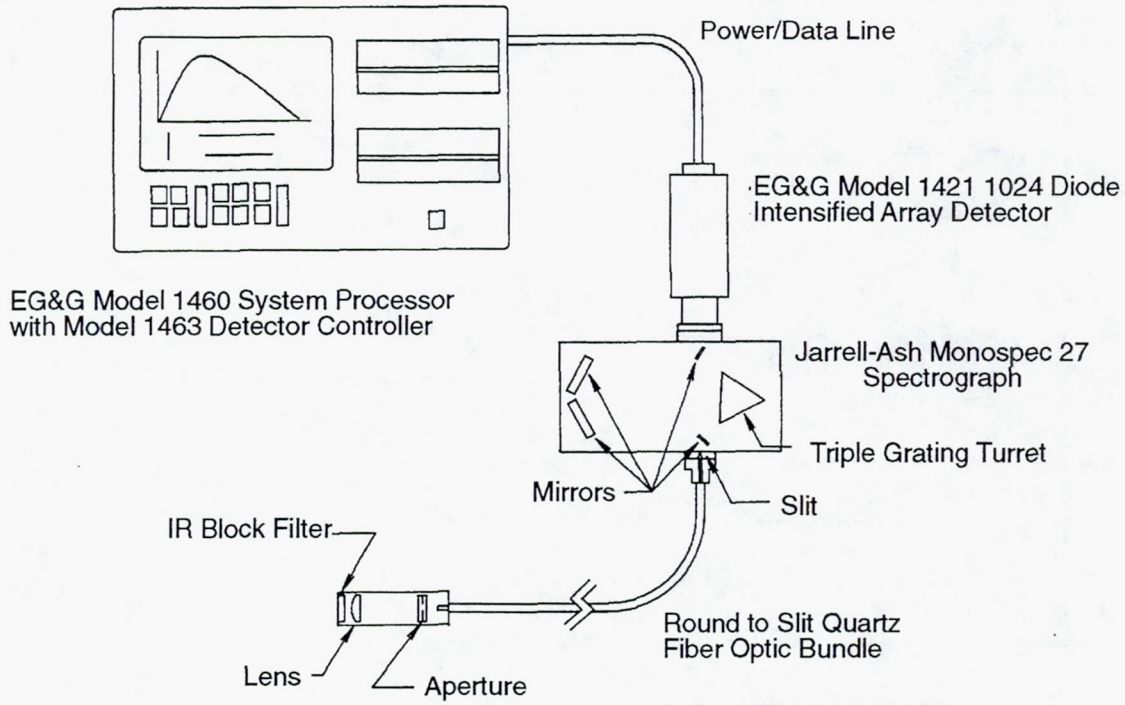

Figure 60. Short Wavelength System Schematic.

round to slit quartz fiber optic cable coupled to a Jarrel Ash Monospec 27 spectrograph. A 1024 element UV enhanced silicon diode array with intensifier plates was located at the focal plane of the spectrograph. The array and diffraction grating combination resulted in a 0.6 nanometer resolution per array element. The array is serially scanned and controlled by an EG&G controller that allows variation of the scan rate and grouping of the array elements. The OMA controller also handles data acquisition. The Metrabyte™ data system described above was not used.

Using the OMA to measure the UV-visible area of the spectrum required changes in the data acquisition programming of the instrument. The time required for a complete scan in the normal operating mode is significant compared with the time required for sample actuation. In order to identify the point at which the radiant energy decay due to positioning outside the zone where reflected energy from the cavity is present and to calculate a correction for the temperature change during actuation, a series of readings must be obtained during the actuation cycle. The unit was programmed to group elements around selected wavelength values and to ignore the remaining elements, which decreased the scan time from 16.6 to 1.45 ms. Several scans were taken and averaged to reduce the high noise (20% variation between consecutive readings on a constant temperature black body) on the signal. The points on the OMA scans were effectively 10 ms apart, which was barely adequate time differentiation. This, combined with the high noise on the system, made the OMA a marginal device for taking emissometer data.

A photomultiplier tube (PMT) with a filter was also tried but rejected because, with available interference filters, the signal-to-noise ratio was not adequate. A PMT and coarse grating monochrometer have been suggested but not tried in the short wavelength regions.

Measurements on the materials using the OMA system have not shown the expected increase in emittance (compared with that measured using a silicon pyrometer). Measurements were performed on three materials (zirconia, 99.8% alumina, and mullite) with measurements taken at 11 equally spaced wavebands surrounding center wavelengths from 0.40 to 0.90 μm. Modifications to the optical system to increase the available energy were made and IR block filters installed in the sight path to reject the large amount of energy from longer wavelengths.

The mullite, zirconia, and alumina samples all showed a flat emissivity versus wavelength relationship in the waveband from 0.4 to 0.9 μm. This is contrary to most published emissivity data on these materials that show a steep increase in emissivity as one approaches 0.40 μm. The OMA data did not agree in the 0.80 to

0.90 μm band with the data obtained from the silicon pyrometer. The emissivities of the ceramics as measured with the OMA were between 0.05 and 0.10 higher than those measured with the silicon pyrometer system. The uncertainty in the measurement due to noise and the slow effective time response of the detector array make it difficult to measure emissivity using this system. A sample OMA plot (***Figure 61***) shows the time response problem and the noise in the measurement system. The slow sampling rate at the top of the curve makes it difficult to determine the point at which the sample began moving That, combined with the noise at the bottom of the curve, makes it difficult to extrapolate to the start of the actuation cycle.

4.5 Analysis

This section contains design considerations for applying long/short wavelength radiation measurements in propulsion systems, the effect of reflected radiation, and the effect of gas emission/absorption.

4.5.1 Design Considerations

A general discussion of the design parameters that apply the long/short wavelength radiation measurement in propulsion systems will be presented. A detailed treatment of the topic is beyond the scope of this program. A recent long wavelength temperature measurement application has been presented to illustrate the magnitude of the problems involved.

4.5.1.1 Long Wavelength Design Considerations

The detectors that operate in this wavelength range are much less stable then silicon detectors. They require cooling to a fixed low temperature, chopping of the incident radiation to provide a stable reference and, even with these provisions, they require frequent calibration. Also, the choices of optical material are severely limited in the wavelength range. These requirements make applications in the typically hot and high vibration propulsion systems extremely difficult.

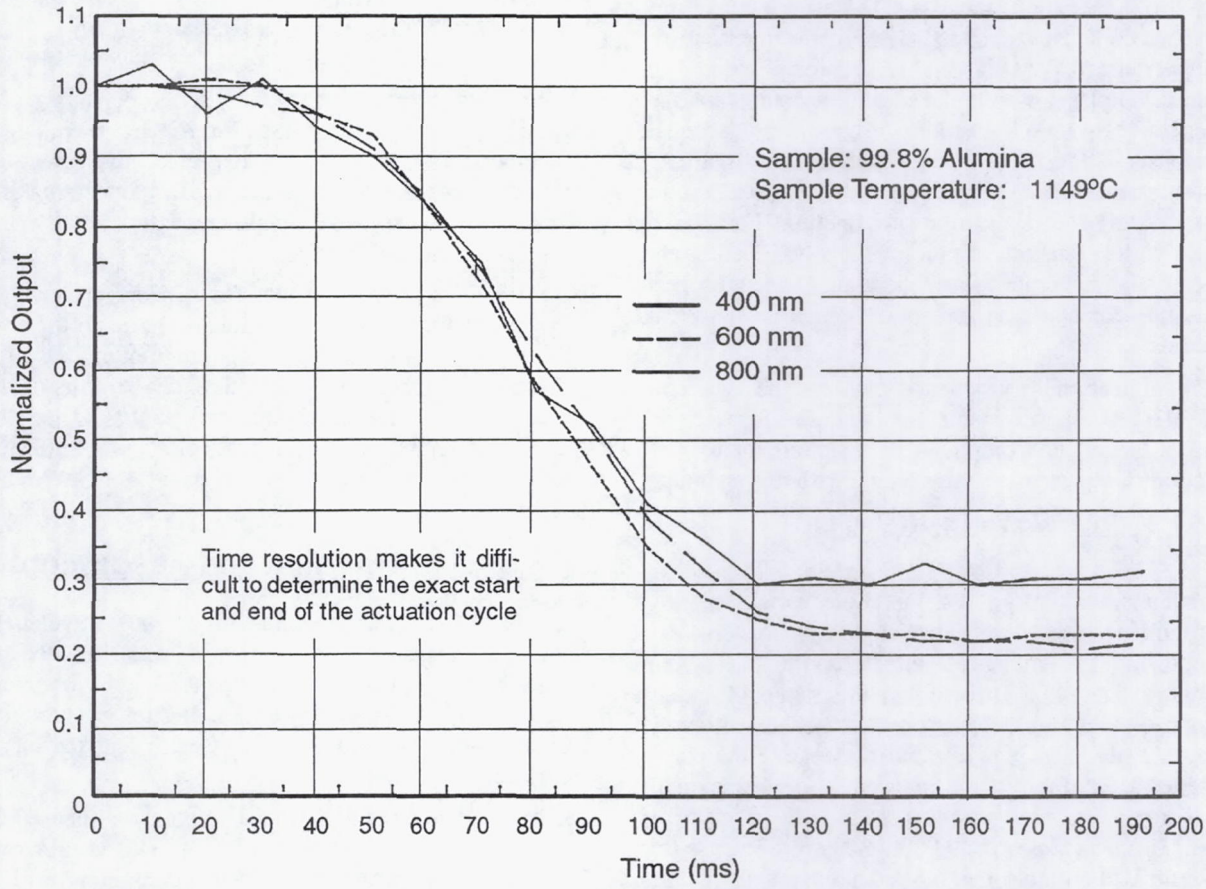

Figure 61. Normalized Optical Multichannel Analyzer Output versus Time.

The following application is provided to show the magnitude of difficulty involved in applying this measurement technique.

4.5.1.2 Long Wavelength Application

The long wavelength pyrometer system described was subsequently used to measure the surface temperature of a zirconia (yttria stabilized) coating applied to a metallic superalloy. The coating was applied to 0.95 cm (0.375 inch) diameter hollow tubes. The tubes were immersed in an atmospheric combustor exhaust plume with cooling air flowing though the tubes. Six tubes were located in a circular pattern 5.7 cm (2.25 inches) in diameter and rotating at up to 1000 rpm. The tube temperature was approximately 1090°C (2000°F). The purpose of this test was to evaluate the coating durability with a temperature gradient across the coating similar to that experienced on jet engine turbine blades. The measurement of the coating surface temperature was required to accurately determine the temperature gradient. A silicon pyrometer was tried for this application but, due to the translucence of the coating, an accurate determination of the surface temperature could not be made.

For this application, the HgCdTe detector was liquid nitrogen cooled and chopped at 3 kHz (the maximum for chopper used). At the higher rotational speeds, the lock-in amplifier was replaced with a computer-based digitizing system in order to obtain an adequate response. The pyrometer was calibrated using a black body source at the approximate tube temperature immediately before and after each reading. Fortunately, there was very little vibration in this application and, because the burner was operating at atmospheric pressure, gas emission/absorption was not a significant factor.

This application is a practical example of the use of long wavelength measurements for ceramic materials and shows the added complications required to make an accurate temperature determination with this technique.

4.5.1.3 Short Wavelength Design Considerations

A number of design considerations would make it difficult to use short wavelength pyrometers as a propulsion system temperature measurement system. Emitted energy in the temperature range of interest drops off very quickly as one approaches ultraviolet wavelengths, and it is difficult to separate the energy emitted at 0.4 μm from the energy at longer wavelengths that are orders of magnitude more intense. (At 1150°C, the 1.0 μm radiance is 19,000 times more intense than 0.4 μm.) Photomultiplier tubes that have high quantum efficiency and can be blind to near infrared and infrared, tend to be temperature-sensitive, electrically unstable, and fragile. Avalanche photodiodes are somewhat noisy and very temperature-sensitive, and the signal from conventional silicon diodes require large amounts of amplification, which tends to increase noise and drift. Quartz, the most commonly used optical material in these wavelengths, is suitable for propulsion system measurements as windows, lenses, or fiber optics.

4.5.2 Reflected Energy

The effect of reflected radiation on temperature determination from radiance measurements can be evaluated using the same method as the Globar reflection calculation. This method was experimentally verified during our testing. ***Figures 62***, ***63***, and ***64*** show the calculated effect for 1.0, 8.65, and 0.4 μm, respectively. The target temperature for the calculations was 1150°C. The reflection source was assumed to have a 0.5 view factor to the target surface, and the data was plotted as a function of reflection source temperature. The emissivity of the reflection source was assumed to be 1.

Figure 62 shows the effect for a silicon pyrometer (1 μm). The metallic superalloy is shown for comparison with current pyrometer applications. As expected, the effect of reflected radiation would be very large for the ceramic materials tested.

Figure 63 shows the effect for a long wavelength pyrometer (8.65 μm). As expected, the effect of reflected radiation has been drastically reduced making this a viable technique for making measurements in the presence of hot adjacent sources.

Figure 64 shows the effect for a short wavelength pyrometer (0.4 μm). Calculations were made for both the emissivities measured in this program and also for those values found in the literature. The results of the measured emissivity are extremely high. Using the published emissivity data, the effect of reflected radiation is also too large to make this a viable technique.

4.5.3 Gas Emission and Absorption

As part of the design evaluation of long wavelength radiation measurement, an effort was initiated to determine a specific wavelength band to avoid absorption and emission by the combustion gas products in the sight path between the detector and the target surface.

The calculations of emission/absorption were based on updated absorption coefficients.[16] This data shows that in the 8 to 10 μm wavelength region there is essentially zero absorption due to carbon dioxide, but

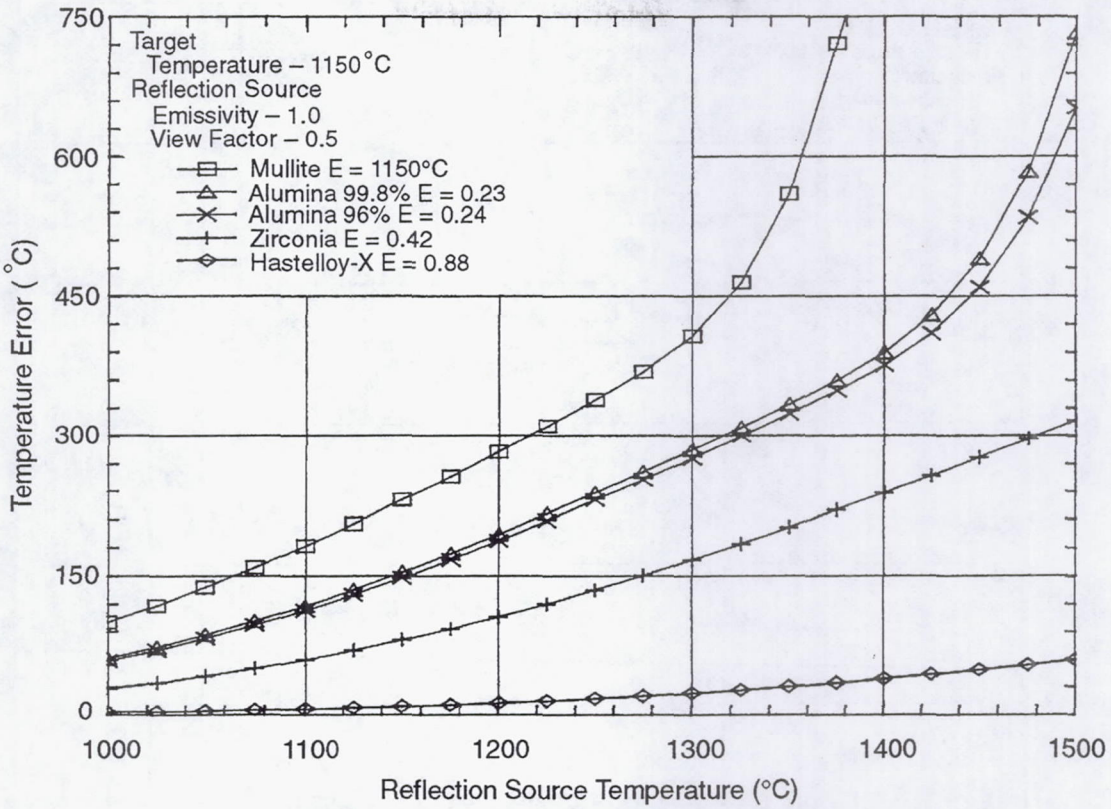

Figure 62. Effect of Reflected Energy – 1.0 μm.

that water vapor absorption is significant. Also, it shows a minimum absorption band for water vapor near 9 μm. We have selected a typical test case (target surface, 1093°C; combustion gas path length, 50 mm; gas path temperature, 1927°C) and calculated the error in indicated target temperature as a function of pressure using the following Beer's Law relationship:

$$a = 1 - e^{-kL}$$

Where

a = spectral absorptivity

k = spectral absorption coefficient

L = optical path length

The results of this calculation are plotted in ***Figure 65*** and show a significant error amounting to approximately 180 K at 30 atmospheres pressure for 4.53% water vapor. The error is positive because the emission from the hotter gas more than makes up for the absorption of energy from the lower temperature target. It should be emphasized that this error is only that due to absorption and emission along the 50 mm combustion gas path length between the target and the detector and does not include other errors caused by reflected radiation or unknown emittance.

Since the magnitude of the error is too large to ignore for most applications, a method for quantitatively defining the error needs to be considered. If the gas path were uniform in temperature, pressure, and constituent proportion along its length (50 mm), it would be possible to calculate the error from local measurements of pressure, temperature, and water content. Lack of uniformity in all of these parameters exists in a real world gas turbine flowpath environment, which complicates the task of assigning a tolerance to the error. We estimate a ~30°C tolerance for the error based on measured local values of pressure, temperature, and water concentrations along the sight path in the combustion gas stream.

4.6 Conclusions

The conclusions can be drawn based on the measurement data and analysis.

4.6.1 Long Wavelength Radiation Measurements

- The materials tested have very high emissivities and are opaque.

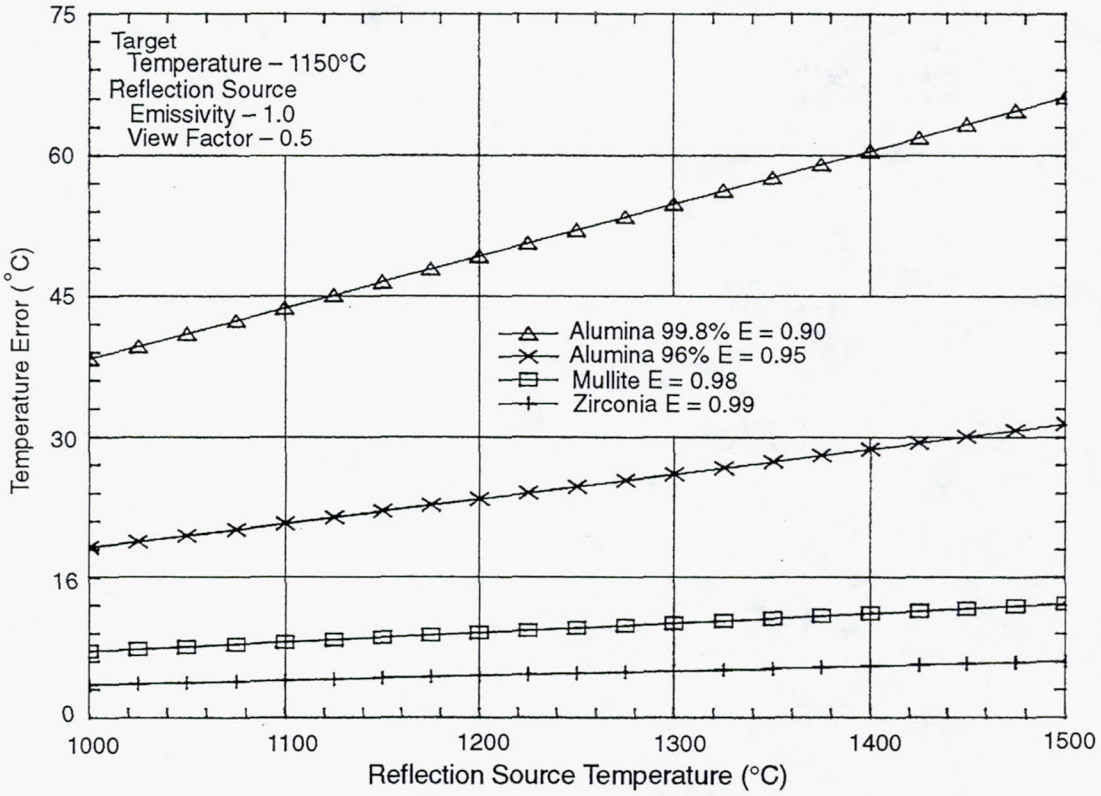

Figure 63. Effect of Reflected Energy – 8.65 μm.

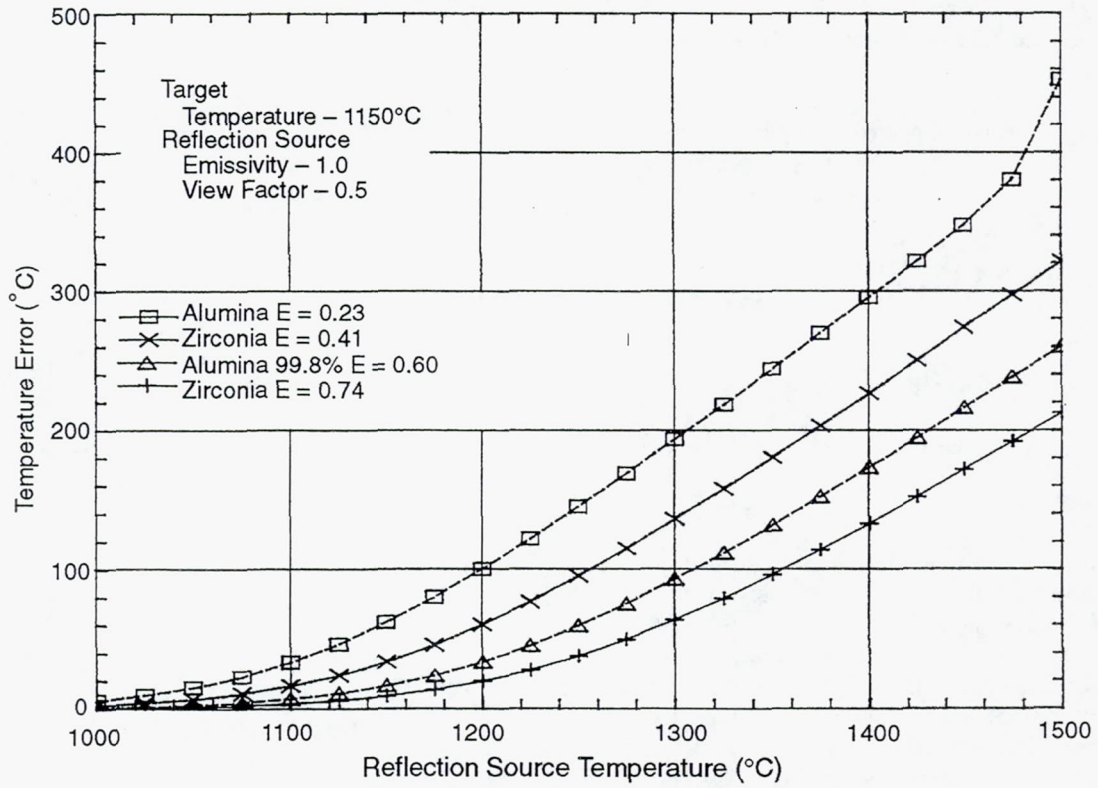

Figure 64. Effect of Reflected Energy – 0.4 μm.

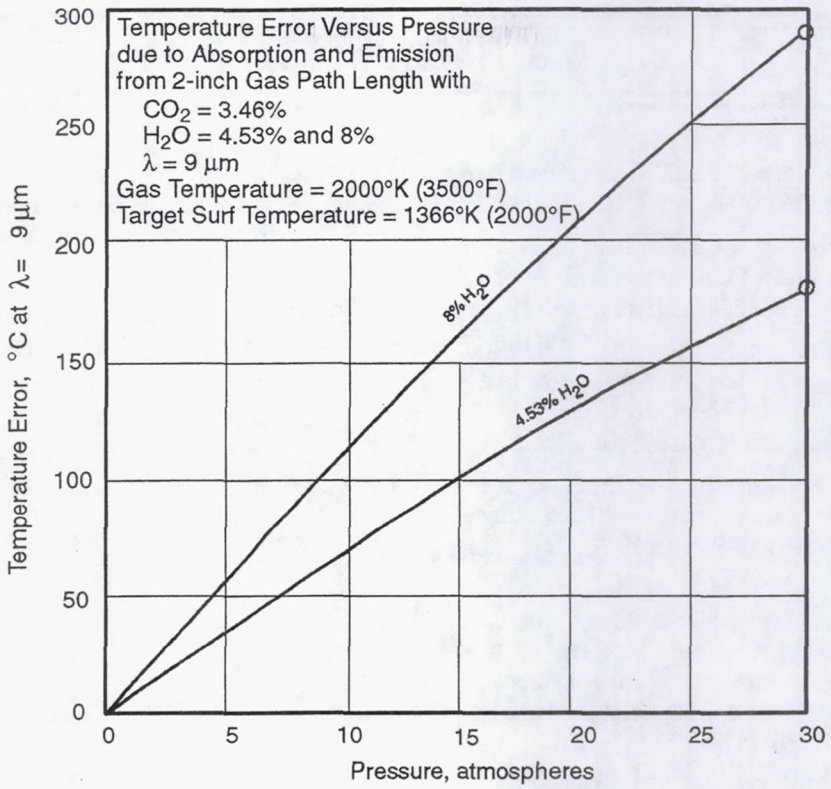

Figure 65. Effect of Gas Emission/Absorption versus Pressure.

- Reflected radiance from adjacent hot parts is not a serious problem.
- Gas emission/absorption is not a serious problem at atmospheric pressure but becomes very significant as pressure increases.
- This technique requires a much more complicated design than silicon pyrometers and is not expected to be as stable.

4.6.2 Short Wavelength Radiation Measurements

- The materials tested did not have a significant increase in emissivity at 0.4 µm. Published data does show an increase.
- Based on the higher published emissivity, reflected radiance from hot parts can cause large errors in temperature measurement.
- Gas emission/absorption is not a problem.
- This technique requires a much more complicated design than silicon pyrometers and is not expected to be as stable.

5.0 References

1. Dils, R.R and Follansbee, P.S., "High Temperature Sputtered Surface Sensors," ISA ASI 75224, 1975.
2. Grant, H.P, Przybyszewski, J.S., Claing, R.G., and Anderson, W.L., "Thin Film Temperature Sensors, Phase III," NASA CR-165476, 1982.
3. Budhani, R.C., Prakash, S., Doerr, H.J., and Bunshah, R.F., "Oxygen Enhanced Adhesion of Platinum Films Deposited on Thermally Grown Alumina Surfaces," J. Vac. Sci. Technol., Nov/Dec 1986.
4. Budhani, R.C., Prakash, S., and Bunshah, R.F., "Thin-Film Temperature Sensors for Gas Turbine Engines: Problems and Prospects," J. Vac. Sci. Technol., Nov/Dec 1986.
5. Holanda, R., Ho., C.H., Prakash, S., and Bunshah, R.F., "Development of Thin-Film Temperature Sensors for Surface Temperature Measurement on High-Temperature Engine Materials," HiTEMP Review, NASA CP-10051, 1990.
6. Atkinson, W.H. and Cyr, M.A., "Evaluation of Sensors for Temperature Measurement of Ceramic Materials," HiTEMP Review, NASA CP-10051, 1990.
7. Samsonov, G.V. and Kisiyi, P.S., "High Temperature Nonmetallic Thermocouples and Sheaths," Consultants Bureau, NY, 1967.
8. Franks, E., "High Temperature Thermocouples using Nonmetallic Members," Temperature, its Measurement and Control in Science and Industry, Vol. 3, Reinhold Pub. Corp., 1962.
9. VonMuench, W. et al., "Preparation of Pure and Doped SiC by Pyrolysis of Silane Compounds," J. Electrochemical Soc., Vol. 125, No. 2, 1978.
10. Bauer, A.A. and Bates, J.L., "An Evaluation of Electrical Insulators for Fusion Reactors," Battelle Memorial Institute, Report BMI, 1930.
11. "Refractory Ceramics for Aerospace," Compiled by Battelle Memorial Inst., Columbus, OH, 1964.
12. Ceramic Data Book, 63rd Edition, 1984.
13. IR&D Project No. 7.14, "Advanced Multicolored Pyrometer."
14. Goldsmith, A., Waterman, T.E., and Hirschhorn, H.J., Handbook of Thermophysical Properties of Solid Materials, Revised Edition, Vol. III: Ceramics, the Macmillan Company, NY, 1961.
15. Ludwig, C.B., Malkmus, W., and Thomson, J.A.L., Handbook of Infrared Radiation from Combustion Gases, NASA SP-3080, 1973.

MAILING LIST

NASA Lewis Research Center
Attn: Daniel Ng (25 copies)
MS 77-1
Cleveland, OH 44135

NASA Lewis Research Center
Attn: Report Control Office
MS 60-1
21000 Brookpark Road
Cleveland, OH 44315

NASA Lewis Research Center
Attn: Library
M. S. 60-3
21000 Brookpark Road
Cleveland, OH 44135

NASA Lewis Research Center
Attn: Wayne Girard
MS 500-305
21000 Brookpark Road
Cleveland, OH 44135

NASA Headquarters
Attn: Pam Richardson
Code R
Washington, DC 20546

NASA Center for Aerospace Information
Attn: Accession Branch (25 copies)
P. O. Box 8757
Baltimore, MD 21240-0757

NASA Marshall Space Flight Center
Attn: William T. Powers
EB-225
Marshall Space Flight Center, AL 35813

NASA Marshall Space Flight Center
Attn: Joseph Zimmerman
Code EB-22
Marshall Space Flight Center, AL 35812

Air Force Wright Aeronautical Laboratory
Attn: William Stange
WL/POTC
Wright Patterson AFB, OH 45433-7251

Air Force Wright Aeronautical Laboratory
Attn: Mr Mervis Schmidt
WL/POTA
Wright Patterson AFB, OH 45433-7251

Arnold Engineering Development Center
DOT
Attn: C. T. Kidd
Air Force Systems Command
Arnold Air Force Station, TN 37389

Arnold Engineering Development Center
Attn: Carlos Tirres
AEDC/XXR
Arnold Air Force Station, TN 37389-1214

Arnold Engineering Development Center
Attn: Gere Matty
AEDC/DOTP
Arnold Air Force Station, TN 37389-1214

Aviation Applied Technology Dir.
Attn: AMSAT-R-TP (Henry Morrow)
Ft. Eustis, VA 23604-5577

Noel Associates
ATTN: B. W. Noel
819 Zia Lane
Española, NM 87532

National Institute of Standards and Technology
Attn: George Burns
Gaithersburg, MD 20899

National Institute of Standards and Technology
Attn: Ken Kreider
221-B312
Gaithersburg, MD 20899

Oak Ridge National Lab
ATTN: M. Cates
P. O. Box 2003
MS 7280
Oak Ridge, TN 37831

Oak Ridge National Lab
ATN: S. Allison
P. O. Box 2003
MS 7280
Oak Ridge, TN 37831

AVCO Lycoming Textron
Lycoming Division
Attn: Steve Curry
Building 6
550 South Main Street
Stratford, CT 06497

Allied Signal Engines
Harvey Niska
P. O. Box 52181
Mail Stop 302-202
Phoenix, AZ 85010

Allied Signal Engines
Attn: Steve Mina
P. O. Box 52181
Mail Stop 302-202
Phoenix, AZ 85010

Allison Engine Co
Attn: Andrew Brewington
MS-W03A
P.O. Box 420
Indianapolis, IN 46206-0420

Allison Engine Co
Attn: Craig Dorste
MS-W03A
P. O. Box 420
Indianapolis, IN 46206-0420

Beamalloy Corp.
Attn: Cliff Lewis
6360 Dublin Industrial Lane
Dublin, OH 43017

Caterpillar Tractor Company
Research Department
Attn: Donald W. Heston
Technical Center, Building L
100 Northeast Adams Street
Peoria, IL 61629

EG&G Energy Measurements, Inc.
ATTN: W. D. Turley
MS 04
130 Robin Hill Road
Goleta, CA 93116

Eaton Corporation
Attn: Les Hayes
Director of Program Development
P. O. Box 766
Southfield, MI 48037

Kaman Sciences Corporation
Attn: Jolene Schneider
1500 Garden of the Gods Rd.
P. O. Box 7463
Colorado Springs, CO 80933-7463

Kulite Semiconductor Products, Inc.
Attn: David Goldstein
One Willow Tree Road
Leonia, NJ 07605

Lewis Engineering Company
Attn: James Dobbs
238 Water Street
Naugatuck, CT 06770

Massachusetts Inst. of Technology
Attn: Alan Epstein
Rm. 31-266
Cambridge, MA 02139

Medtherm Corp
Attn: Larry Jones
27604 Newby Rd
Huntsville, AL 35805

Orbital Technologies Corporation
Attn: Eric E. Rice
402 Gammon Place, Suite 10
Madison, WI 53719

PRC System Service
Attn: M. M. Lemcoe
P. O. Box 273
Facility Support Complex (FSC)
Edwards, CA 93523-5000

Public Service Elect. & Gas Company
Attn: Melvin L. Zwillenberg
Research & Development Dept.
80 Park Plaza
Newark, NJ 07101

RdF Corporation
Attn: Frank Hines
P. O. Box 490
23 Elm Avenue
Hudson, NH 03051

Rockwell International
Rocketdyne Division
Attn: Sarkis Barkhoudarian
6633 Canoga Avenue
Canoga Park, CA 91303

Rosemont, Inc.
Technical Library
Attn: Carolyn Hagford, Mail Stop
FL-21
P.O. Box 959
14300 Judicial Road
Burnsville, MN 55306

Spire Corporation
ATTN: Charles Blatchley
One Patriot Park
Bedford, MA 01730-6000

Spire Corporation
Attn: Roger G. Little
One Patriots Park
Bedford, MA 01730-2396

Stanford University
Attn: R. J. Moffatt
Asst. Prof., Mech. Engr.
Thermosciences Division
Stanford, CA 94305

Stein Engineering Services, Inc.
Attn: Peter K. Stein
5602 East Monte Rosa
Phoenix, AZ 85018-4646

Teledyne CAE
Attn: Marlene Dondell, Librarian
1330 Laskey Road
Toledo, OH 43612-0971

Thermogage, Inc.
Attn: Charles E. Brookley
330 Allegany Street
Frostburg, MD 21534

Titan Spectron
Attn: Pete Kenefick
1582 Parkway Loop
Suite B
Tustin, CA 92680

University of California, Los Angeles
Attn: Prof. R.F. Bunshah
Dept. of Materials Science and Engineeri
6532 Boelter Hall
Los Angeles, CA 90024

University of Rhode Island
Attn: Prof. Otto Gregory
Room 110 Crawford Hall
Dept Chemical Engineering
Kingston, RI 02881

Williams International
Attn: Lance Shew
MS 4-10
P.O. Box 200
Walled Lake, MI 48390-2052

United Technologies Corp.
Pratt & Whitney Aircraft
Attn: W. Barry Lunn
Main Plant MS 716-87
P. O. Box 109600
West Palm Beach, FL 33410

United Technologies Corp.
Pratt & Whitney
Attn: Ernesto Suzrez, MS 716-87
Main Plant
P. O. Box 109600
West Palm Beach, FL 33410

United Technologies Corporation
Pratt and Whitney Aircraft
Attn: William H. Atkinson
MS 116-01
400 Main Street
East Hartford, CT 06108

United Technologies Corporation
Pratt and Whitney
Attn: Kenneth Benson
Engineering Division, MS 161-21
400 Main Street
East Hartford, CT 06108

REPORT DOCUMENTATION PAGE

Form Approved
OMB No. 0704–0188

Public reporting burden for this collection of information is estimated to average 1 hour per response, including the time for reviewing instructions, searching existing data sources, gathering and maintaining the data needed, and completing and reviewing the collection of information. Send comments regarding this burden estimate or any other aspect of this collection of information, including suggestions for reducing this burden, to Washington Headquarters Services, Directorate for Information Operations and Reports, 1215 Jefferson Davis Highway, Suite 1204, Arlington, VA 22202–4302, and to the Office of Management and Budget, Paperwork Reduction Project (0704–0188), Washington, DC 20503.

1. AGENCY USE ONLY *(Leave Blank)*	2. REPORT DATE	3. REPORT TYPE AND DATES COVERED
	1 August 1995	Final — April 87 – August 94

4. TITLE AND SUBTITLE

Sensors for Ceramic Components in Advanced Propulsion Systems

5. FUNDING NUMBERS

WU–505–62–50
WU–505–63–12
C–NAS3–25140

6. AUTHOR(S)

A.C. Koller, W.H. Bennethum, S.D. Burkholder, R.R. Brackett, and J.P. Harris

7. PERFORMING ORGANIZATION NAME(S) AND ADDRESS(ES)

GE Aircraft Engines
Product Test Center
One Neumann Way
Cincinnati, OH 54215–6301

8. PERFORMING ORGANIZATION REPORT NUMBER

E–9273

9. SPONSORING/MONITORING AGENCY NAME(S) AND ADDRESS(ES)

National Aeronautics and Space Administration
Washington, D.C. 20546–0001

10. SPONSORING/MONITORING AGENCY REPORT NUMBER

NASA CR–195410

11. SUPPLEMENTARY NOTES

Project Manager, Daniel L. Ng, Instrumentation and Control Technology Division, NASA–Lewis Research Center, organization code 2510, (216) 433–3638.

12a. DISTRIBUTION/AVAILABILITY STATEMENT

Unclassified - Unlimited
Subject Category 35

12b. DISTRIBUTION CODE

13. ABSTRACT *(Maximum 200 words)*

This report includes:

1. A survey of the current methods for the measurement of surface temperature of ceramic materials suitable for use as hot section flowpath components in aircraft gas turbine engines
2. Analysis and selection of three sensing techniques with potential to extend surface temperature measurement capability beyond current limits
3. Design, manufacture, and evaluation of the three selected techniques which include the following:
   - Platinum rhodium thin film thermocouple on alumina and mulite substrates
   - Doped silicon carbide thin film thermocouple on silicon carbide, silicon nitride, and aluminum nitride substrates
   - Long and short wavelength radiation pyrometry on the substrates listed above plus yttria stabilized zirconia

Measurement of surface emittance of these materials at elevated temperature was included as part of this effort.

14. SUBJECT TERMS

Temperature; Sensors; Ceramics; Propulsion systems; Thin film

15. NUMBER OF PAGES

46

16. PRICE CODE

17. SECURITY CLASSIFICATION OF REPORT	18. SECURITY CLASSIFICATION OF THIS PAGE	19. SECURITY CLASSIFICATION OF ABSTRACT	20. LIMITATION OF ABSTRACT
Unclassified	Unclassified	Unclassified	UL